

Supplementary information

Lithium-excess olivine electrode for lithium rechargeable batteries

Kyu-Young Park, Inchul Park, Hyungsub Kim, Gabin Yoon, Hyeokjo Gwon, Yongbeom Cho,
Young Soo Yun, Jung-Joon Kim, Seongsu Lee, Docheon Ahn, Yunok Kim, Haegyeom Kim,
Insang Hwang, Won-Sub Yoon and Kisuk Kang

*Corresponding e-mail: matlgen1@snu.ac.kr

Detailed synthetic process of lithium-excess LFP

i) Each precursor powders, such as Li_2CO_3 , $\text{FeC}_2\text{O}_4 \cdot \text{H}_2\text{O}$ and $(\text{NH}_4)\text{HPO}_4$, is pulverized as fine as possible, separately. In this process, we usually used high energy ball milling at Ar atmosphere to avoid the oxidation. Especially, the phosphorus precursor should be carefully handled because it easily transforms to glass or bulk-like powder in a short time under the moisture condition.

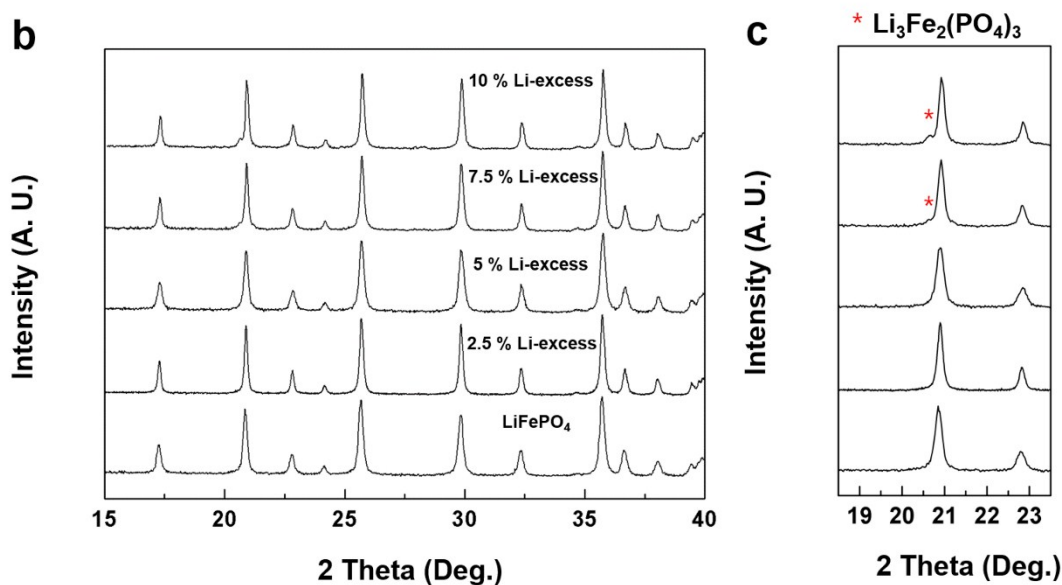
ii) The fine precursors are mixed by wet ball milling more than 24 hours before the calcination process. With less than 24 hours of mixing, the lithium-excess phase is not well formed after the sintering process.

iii) The mixed powder by wet ball-milling is dried at 120 °C. And, the dried powder is, again, pulverized as fine as possible using dry ball milling to obtain uniformity. After that, the powder is calcinated at 350 ° C with 5 ~ 6 °C/min heating rate for 10 hours.

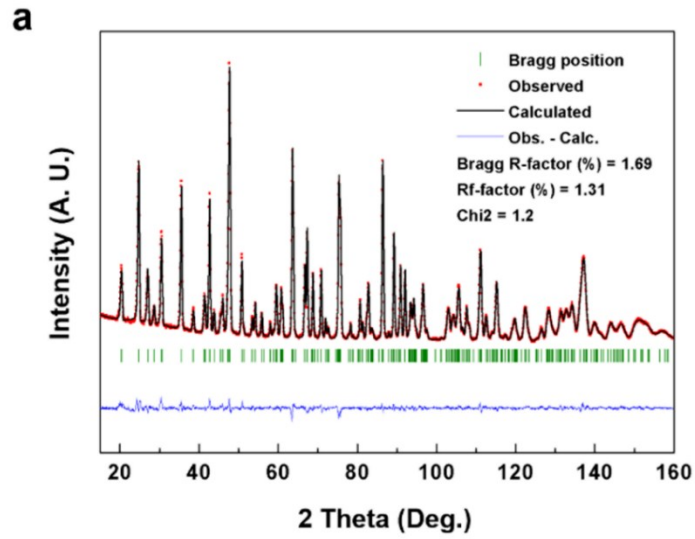
iii) Before the sintering process, all calcinated powder is pulverized. Then, the powder is pelletized under more than 300 bar. The sintering is conducted with relatively fast heating rate at a 5 ~ 6 ° C/min rate in Ar atmosphere.

a

Method	Li : Fe : P ratio	Temperature (°C)	Reaction Time (hour)	Atmosphere	Crystalline impurity
Solid-state	1.025 : 0.975 : 1	600	10	Ar	-
Solid-state	1.05 : 0.95 : 1	600	10	Ar	-
Solid-state	1.075 : 0.925 : 1	600	10	Ar	Li ₃ Fe ₂ (PO ₄) ₃
Solid-state	1.1 : 0.90 : 1	600	10	Ar	Li ₃ PO ₄ /Li ₃ Fe ₂ (PO ₄) ₃
Solid-state	1.05 : 0.95 : 1	700	10	Ar	Li ₃ PO ₄ /Li ₃ Fe ₂ (PO ₄) ₃
Solid-state	1.05 : 0.95 : 1	800	10	Ar	Li ₃ PO ₄ /Li ₃ Fe ₂ (PO ₄) ₃
Hydrothermal	3.0 : 0.95 : 1	180	4	Ar	Li ₃ PO ₄ /Li ₃ Fe ₂ (PO ₄) ₃
Hydrothermal	3.0 : 0.95 : 1	200	4	Ar	Li ₃ PO ₄ /Li ₃ Fe ₂ (PO ₄) ₃
Hydrothermal	3.0 : 0.95 : 1	220	4	Ar	Li ₃ PO ₄ /Unknown impurity



S Figure 1. (a) Various synthetic condition and the impurity of each conditions (b) XRD patterns of 0, 2.5, 5, 7.5 and 10 % Li-excess composition of olivine synthesized through solid-state method. (c) Magnified of 18 ~ 24 ° of XRD patterns. The stoichiometric (0% Li-excess) and 5 % Li-excess composition show no crystalline impurities, but the 7.5 % and 10 % contain Li₃Fe₂(PO₄)₃ impurities. (Measurement condition: range 15 ~ 40 °, step size 0.02 °, by D2 phaser, Bruker)

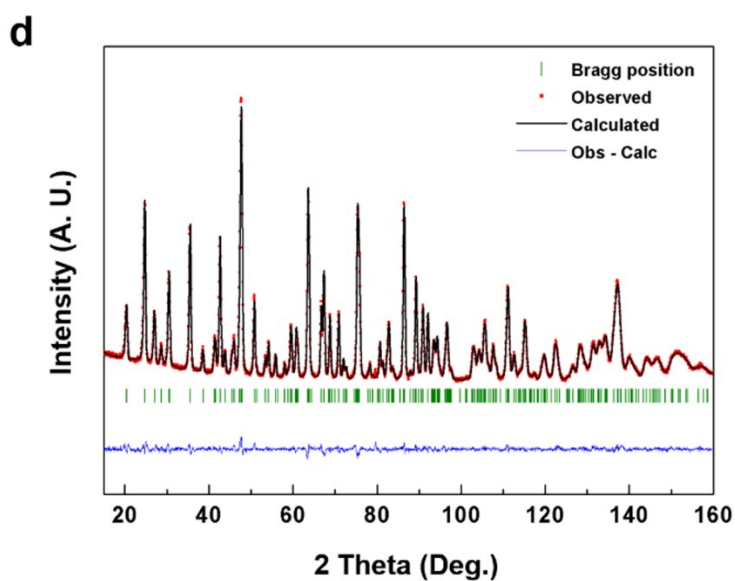


b

	$U_{11} / \text{\AA}^2$	$U_{22} / \text{\AA}^2$	$U_{33} / \text{\AA}^2$	$U_{12} / \text{\AA}^2$	$U_{13} / \text{\AA}^2$	$U_{23} / \text{\AA}^2$	Isotropic therm. Fact
Li	61.1	58.4	127.8	10.6	-9.3	-27.8	1.137
S. D.	4.6	11.8	21.6	5.5	12	12.7	74
Li _{Fe}	10.6	59.1	27.7	0	-0.2	0	0.436
S. D.	0.8	2.4	4.4	0	1.6	0	12
Fe	10.6	59.1	27.7	0	-0.2	0	0.436
S. D.	0.8	2.4	4.4	0	1.6	0	12
Fe _{Li}	61.1	58.4	127.8	10.6	-9.3	-27.8	1.137
S. D.	4.6	11.8	21.6	5.5	12	12.7	74
P1	31.2	63.6	91.9	0	6.5	0	0.729
S. D.	1.7	4.1	7.8	0	3.3	0	23
O1	30.7	60.9	81.8	0	-6.5	0	0.652
S. D.	1.3	3.8	6.8	0	2.8	0	20
O2	29.7	89.4	107.1	0	11.3	0	0.771
S. D.	1.6	4.3	8.7	0	2.9	0	24
O3	27.8	75.3	107.1	10	16.1	-7.7	0.782
S. D.	1	2.5	5.3	1.6	2	3.1	15

c

Name	x (Å)	y (Å)	z (Å)	Occ.
Li	0	0	0	1.000(2)
Li _{Fe}	0.28184(9)	0.25	0.9732(3)	0.042(2)
Fe	0.28184(9)	0.25	0.9732(3)	0.958(2)
Fe _{Li}	0	0	0	0.000(2)
P1	0.09444(17)	0.25	0.4177(3)	1
O1	0.09791(17)	0.25	0.7402(4)	1
O2	0.45748(15)	0.25	0.2043(4)	1
O3	0.16493(14)	0.04736(19)	0.2848(2)	1



e

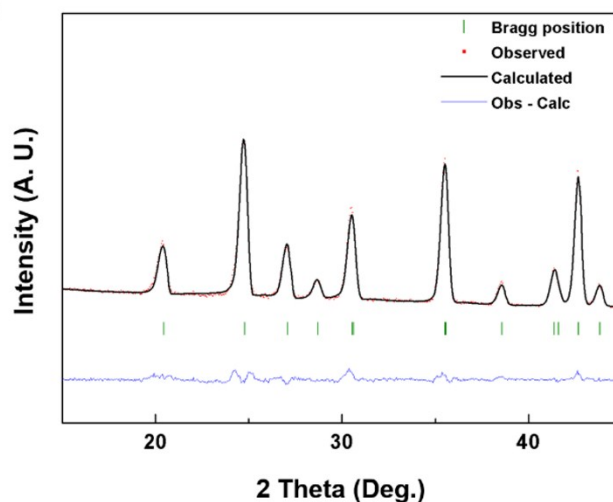
	U23 / Å ²	U22 / Å ²	U33 / Å ²	U12 / Å ²	U13 / Å ²	U23 / Å ²	Isotropic therm. Fact
Li	37.5	83.9	33.6	7.4	13.1	-2.5	1.063(80)
S.D.	5.3	15.4	23.6	6.5	13.8	15.5	
Li _{Fe}	7.7	46.3	76.3	0	-0.6	0	0.628(13)
S.D.	0.9	2.8	4.7	0	1.8	0	
Fe	7.7	46.3	76.3	0	-0.6	0	0.628(13)
S.D.	0.9	2.8	4.7	0	1.8	0	
Fe _{Li}	37.5	83.9	33.6	7.4	13.1	-2.5	1.063(80)
S.D.	5.3	15.4	23.6	6.5	13.8	15.5	
P1	15.3	30.3	37.6	0	4.5	0	0.415(20)
S.D.	1.8	4.6	8.4	0	3.7	0	
O1	10.9	18	21.8	0	-3.3	0	0.508(25)
S.D.	1.3	4.1	7.4	0	3	0	
O2	10.6	28.9	33.6	0	-2.6	0	0.583(15)
S.D.	1.7	4.6	9.5	0	3.1	0	
O3	10.8	35.5	41.6	11.2	7.7	-2.7	0.628(13)
S.D.	1.1	2.7	5.8	1.8	2.2	3.4	

f

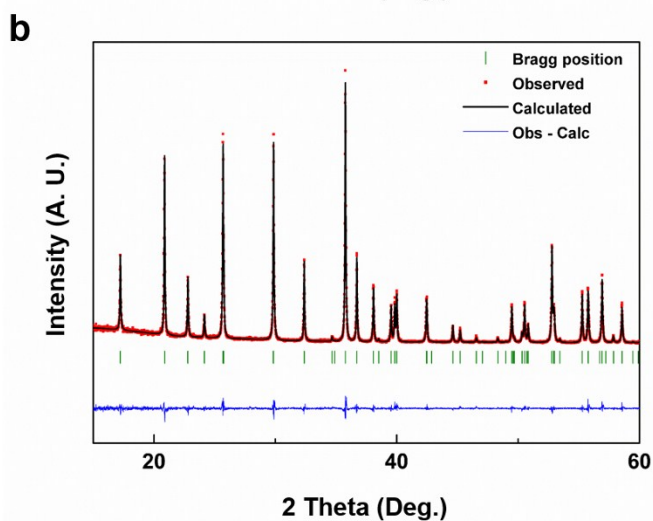
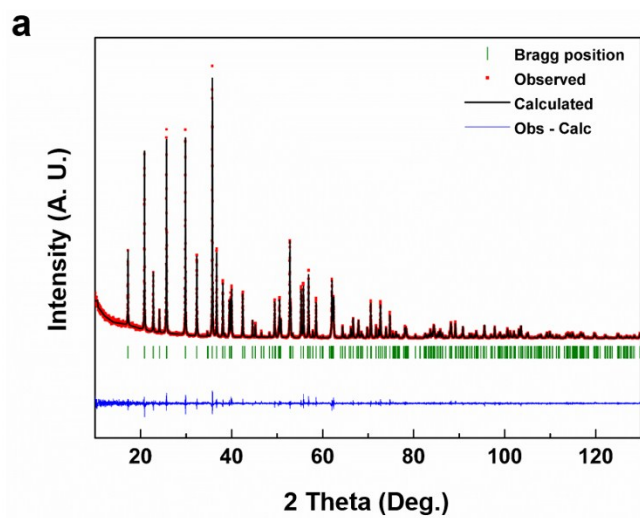
Name	x (Å)	y (Å)	z (Å)	Occ.
Li	0	0	0	0.994(2)
Li _{Fe}	0.28201(10)	0.25	0.9738(3)	0.006(2)
Fe	0.28218(6)	0.25	0.97469(15)	0.994(2)
Fe _{Li}	0	0	0	0.006(2)
P1	0.09515(19)	0.25	0.4175(4)	1
O1	0.09758(19)	0.25	0.7406(4)	1
O2	0.45744(16)	0.25	0.2048(4)	1
O3	0.16476(15)	0.0472(2)	0.2850(3)	1

g

Sample	Li-LiFePO ₄	Li-Li _{1.05} Fe _{0.95} PO ₄
Crystal system	Orthorhombic	
Space group	Pnma (No. 62)	
Lattice parameters		
<i>a</i> (Å)	10.32369(13)	10.32719(11)
<i>b</i> (Å)	6.00555(8)	6.00707(7)
<i>c</i> (Å)	4.69318(6)	4.69227(5)
Unit cell volume (Å ³)	290.974(6)	291.090(5)
Source	Neutron	
Temperature (K)	300	
Wavelength (Å)	1.83432	
2θ range	0 - 160 °	
Number of data positions	3200	
Bragg R-factor (%)	1.35	1.58
Rf-factor (%)	0.847	1.09
Chi ²	2.3	2.99

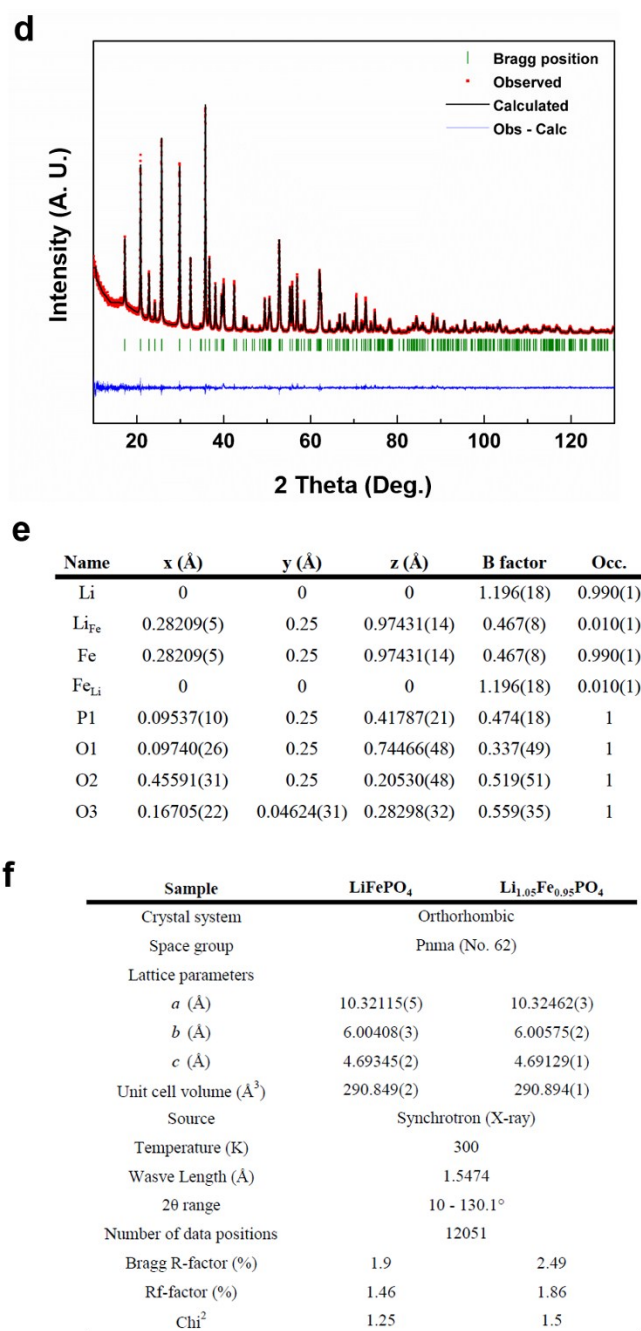
h

S Figure 2. Neutron diffraction (ND) Rietveld refinement results of (a) - (c) lithium-excess LFP and (d) - (f) normal LFP. Figure (g) shows overall crystal structure factors and refinement information. The excessive Li ions are positioned at M2 octahedral site with 4.2 % occupancy. Also, the anti-site is not observed at Li-excess LFP. Figure (h) shows zoomed-in figure of (a). (Wyckoff of each sites; Li and Fe_{Li}: 4*a*; Fe, Li_{Fe}, P, O1 and O2: 4*c*; O3: 8*d*)

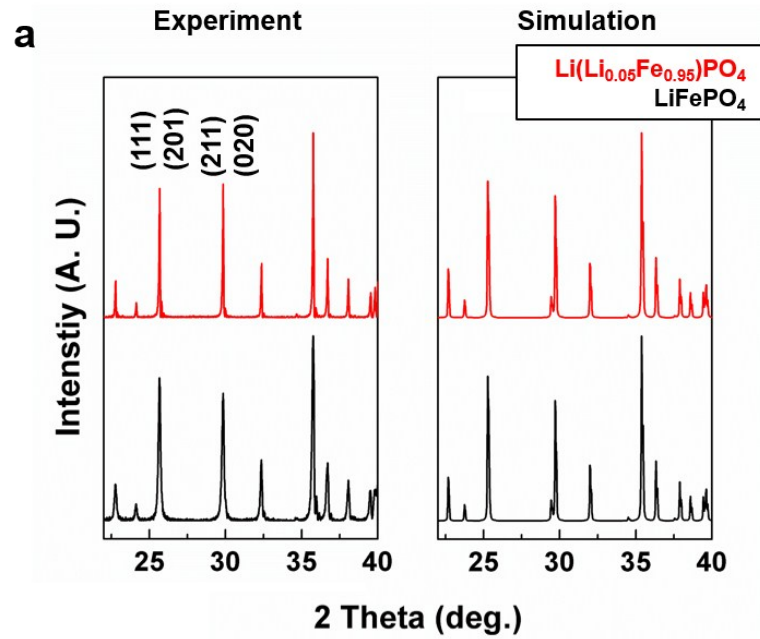


c

Name	x (Å)	y (Å)	z (Å)	B factor	Occ.
Li	0	0	0	1.240(20)	1.000(0)
Li _{Fe}	0.28230(6)	0.25	0.97451(14)	0.425(9)	0.044(0)
Fe	0.28230(6)	0.25	0.97451(14)	0.425(9)	0.956(0)
Fe _{Li}	0	0	0	1.240(20)	0.000(0)
P1	0.09520(10)	0.25	0.41754(22)	0.691(20)	1
O1	0.09706(27)	0.25	0.74535(51)	0.638(55)	1
O2	0.45541(30)	0.25	0.20528(51)	0.795(58)	1
O3	0.16631(22)	0.04554(31)	0.28342(34)	0.755(39)	1



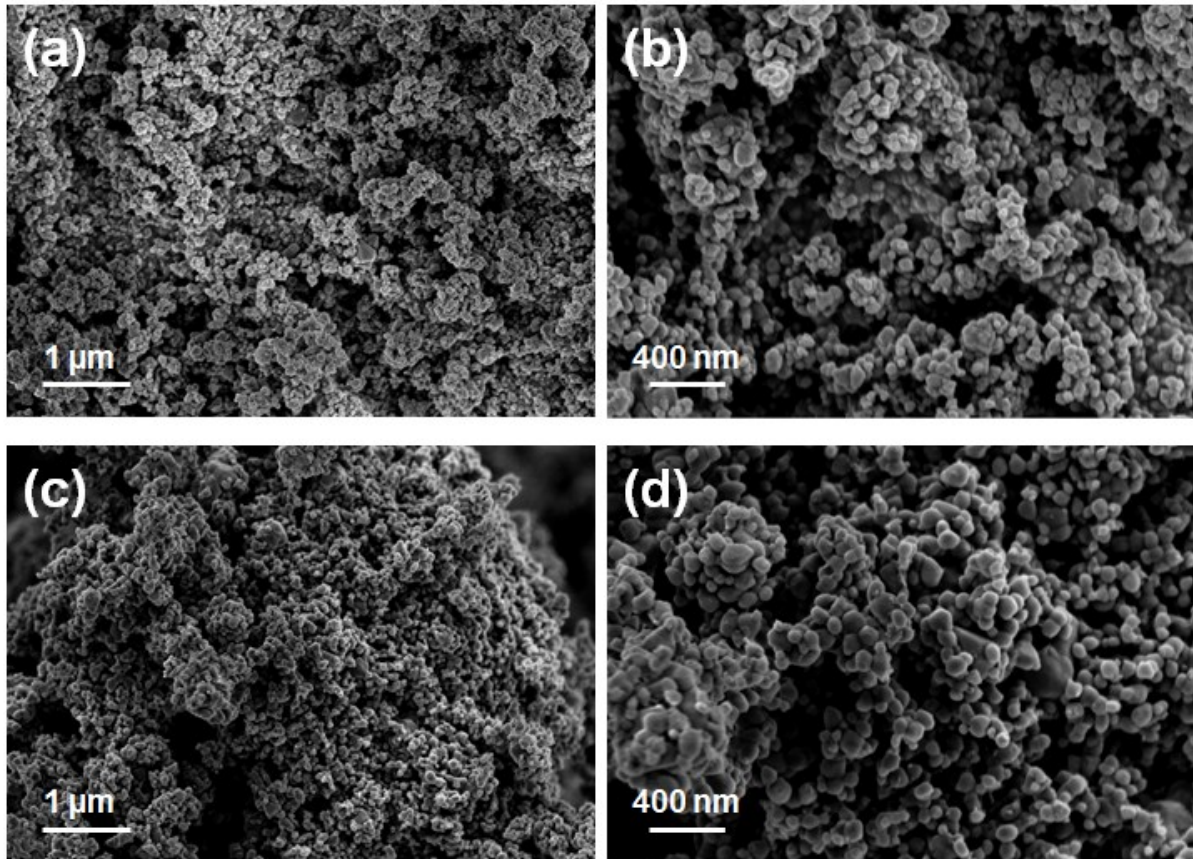
S Figure 3. XRD Rietveld refinement results of (a) - (c) lithium-excess LFP and (d) - (e) normal LFP. Figure (f) shows overall crystal structure factors and refinement information. The high resolution XRD Rietveld refinement results are consistent with ND refinement results of zero anti-site in Li-excess phase. (Wyckoff of each sites; Li and Fe_{Li}: 4a; Fe, Li_{Fe}, P, O1 and O2: 4c; O3: 8d)



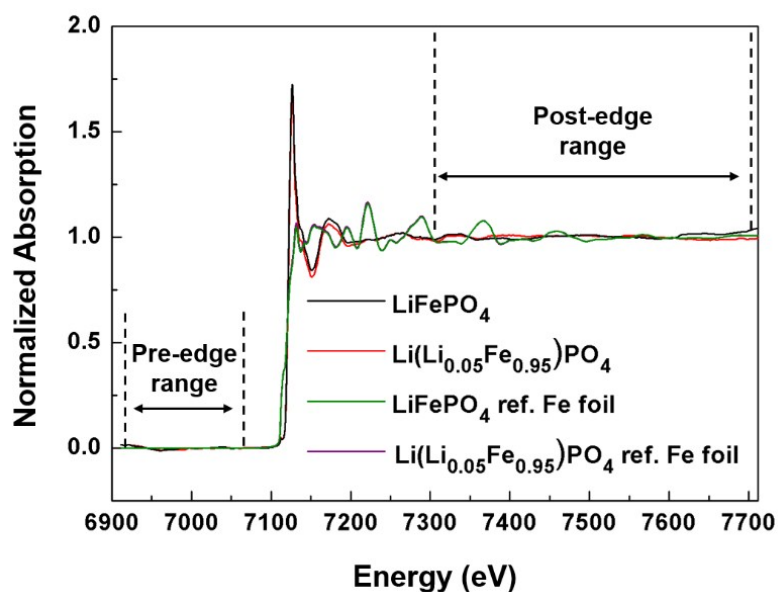
b

Sample	(211) (020)	/	(111) (201)	Condition
$\text{Li}(\text{Li}_{0.05}\text{Fe}_{0.95})\text{PO}_4$		1.05		Exp.
LiFePO_4		0.86		Exp.
$\text{Li}(\text{Li}_{0.05}\text{Fe}_{0.95})\text{PO}_4$		0.95		Simul.
LiFePO_4		0.83		Simul.

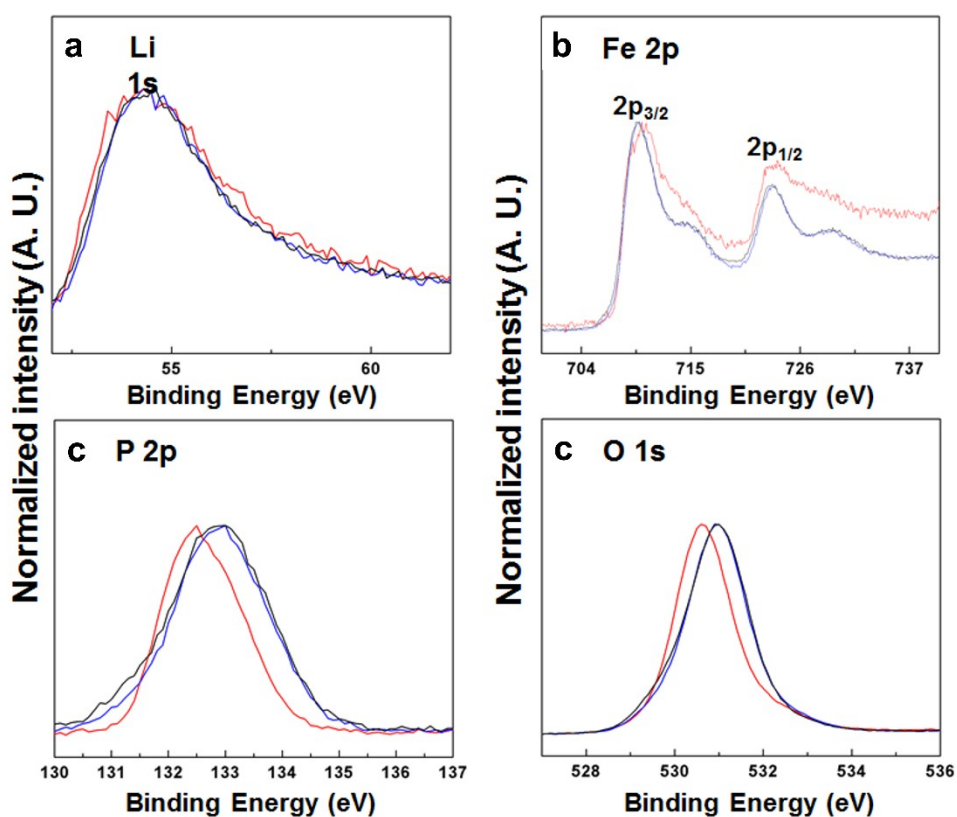
S Figure 4. High resolution XRD experiment and simulation results (a). We conduct XRD simulation for confirming how the XRD peak intensity ratio change at lithium-excess LFP with zero anti-site. Left figure in (a) shows the experiment result and right figure shows the simulation result. The intensity ratio of (111)(201) and (211)(020) is mainly change at both experiment and simulation results as exhibited in table (b).



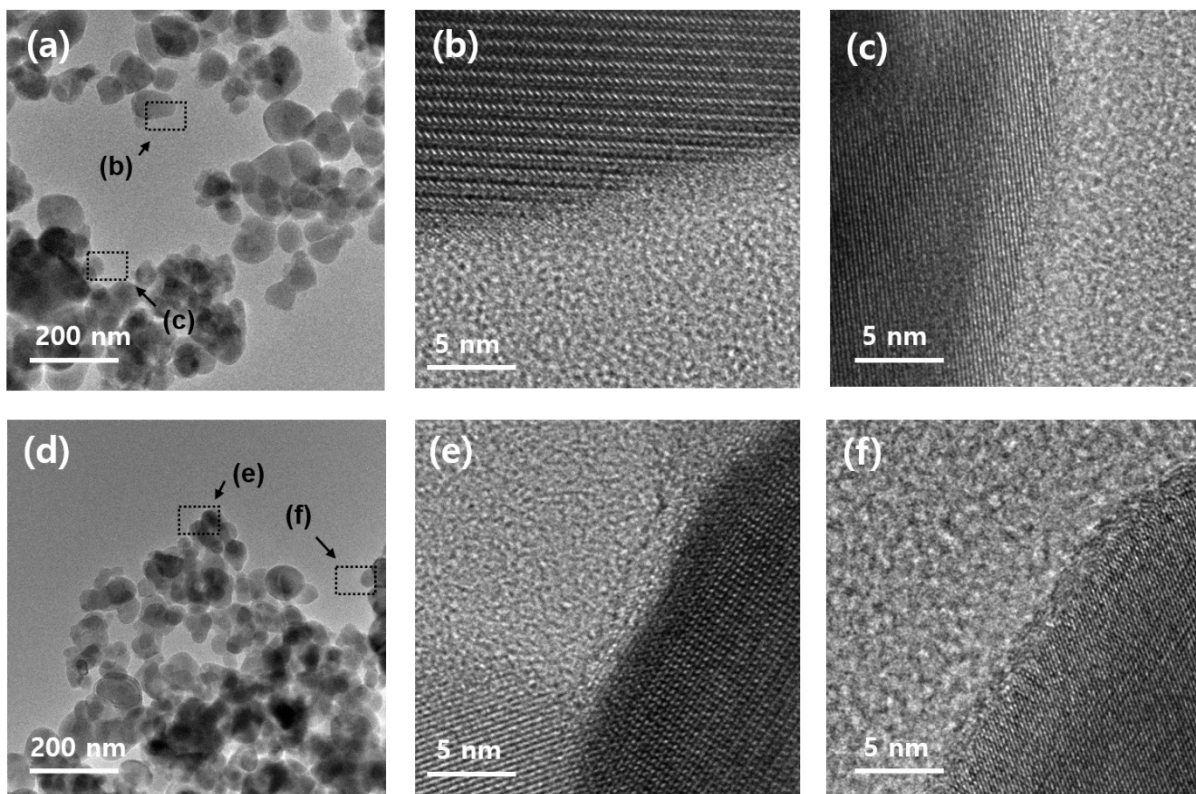
S Figure 5. SEM image of normal and 5 % lithium-excess LFPs. The figure (a) and (b) show normal LFP. The figure (c) and (d) show 5 % lithium-excess LFP. The particle size of Li-excess LFP (~ 150 nm) is slightly higher than normal LFP (~ 100 nm).



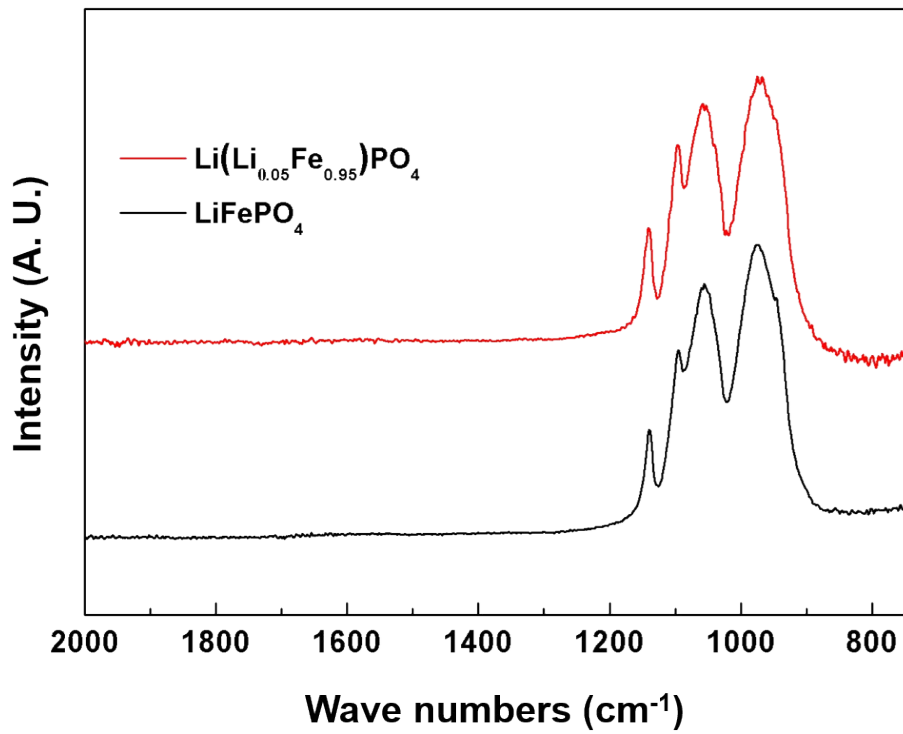
S Figure 6. XANES analysis of lithium-excess and normal LFPs with reference Fe foils. The pre- and post-edge ranges for normalization are applied with 6912 ~ 7062 eV and 7312 ~ 7712 eV, respectively. The Fe reference foils are simultaneously measured for accurate analysis. The reference Fe foils are perfectly overlapped at both measurement. It indicates well align zero shift during measurement.



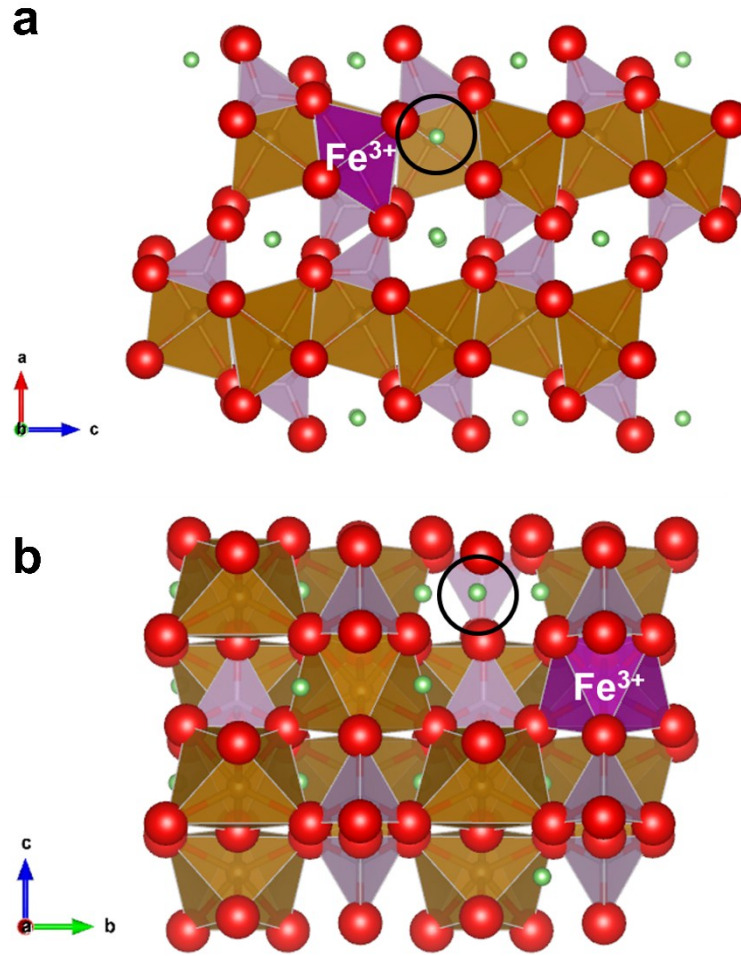
S Figure 7. Surface analysis on after 700 °C annealed lithium-excess LFP (red line) and normal LFP (black line). The blue lines show 10 nm etched surface analysis of lithium-excess LFP. (a) Li 1s XPS (b) Fe 2p XPS (c) P 2p XPS and (d) O 1s XPS. After heat treatment at 700 °C, the lithium-excess LFP shows different signal when compared with normal LFP and that of etched surface. It is caused by impurities of Li_3PO_4 and $\text{Li}_3\text{Fe}_2(\text{PO}_4)_3$ as shown in S Figure 12. Heat treatment XPS results indicates that the Li-excess phase is broken when it heated at high temperature.



S Figure 8. The figure exhibits the TEM images of lithium-excess ((a), (b) and (c)) and normal LFP ((d), (e), and (f)). The (b), (c) and (e), (f) images are magnified boxes in figure (a) and (d), respectively. Both LFPs show that the amorphous phase is unidentifiable at the surface and in the bulk.

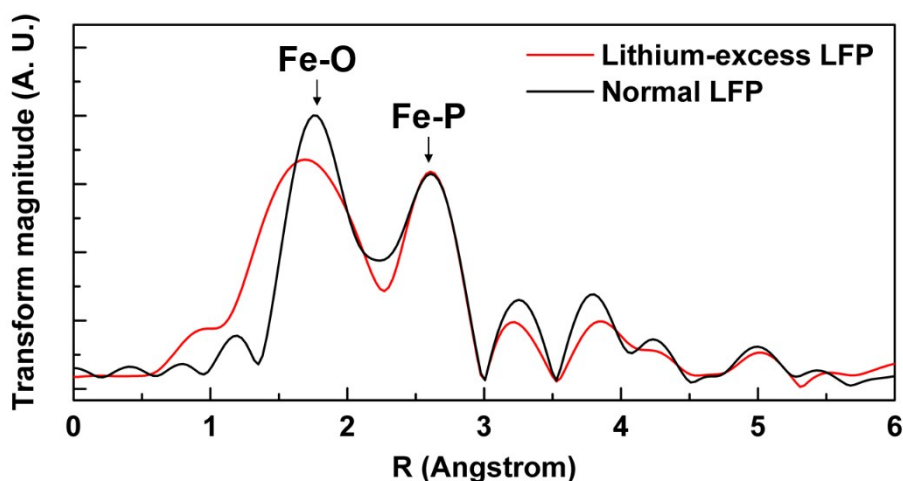


S Figure 9. Fourier transform infrared spectroscopy (FT-IR) results of lithium-excess (red) and normal LFPs (black). Both materials does not show any impurities signal.

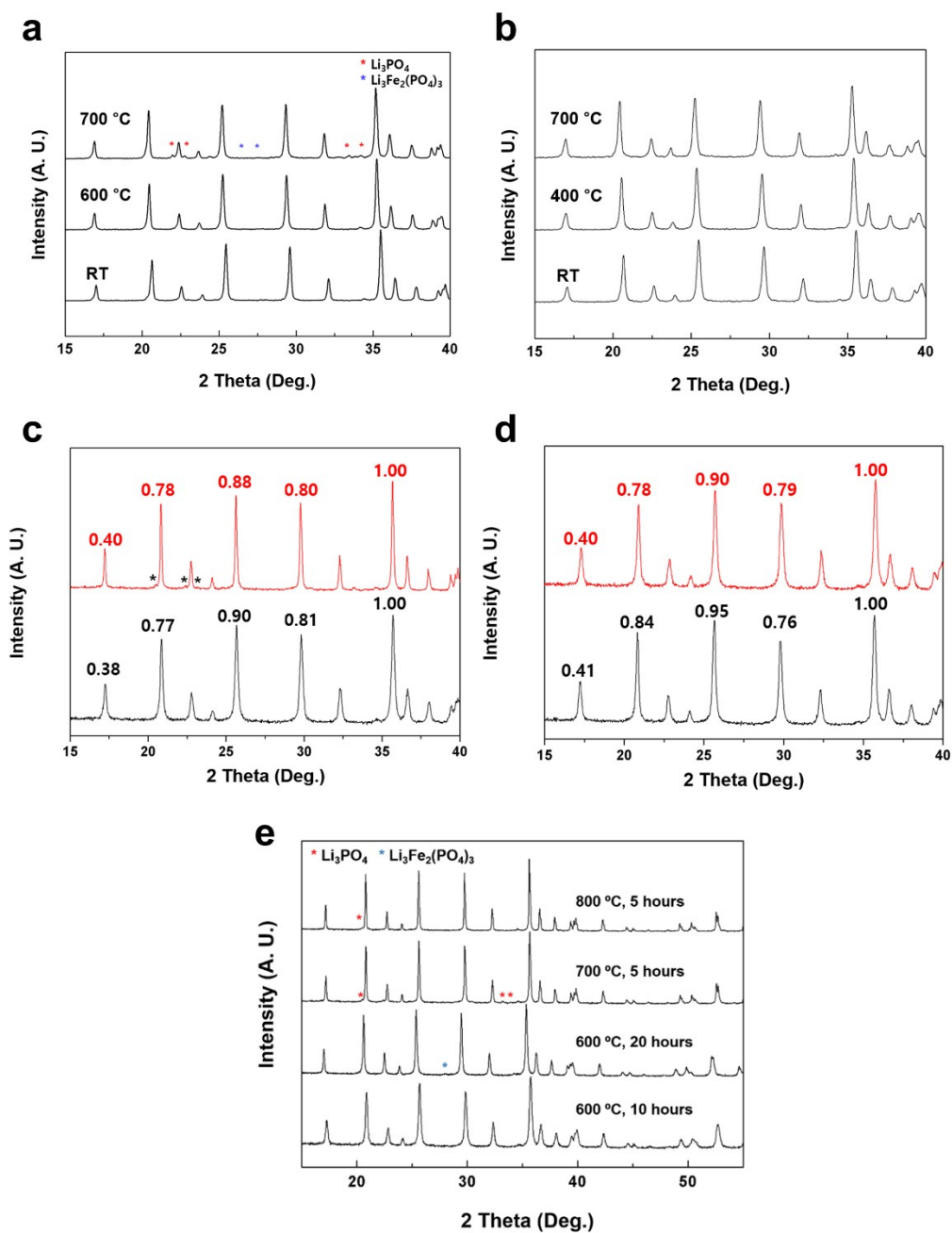


S Figure 10. The most stable lithium-excess configuration calculated by DFT calculation tool along (a) *b*- and (b) *a*-axis. One Fe ion has 3+ oxidation state. (brown octahedron: Fe²⁺, purple octahedron: Fe³⁺, light purple tetrahedron: P, green atom: lithium and red atom: oxygen). The black circle indicates the lithium-excess ion. DFT calculations were performed using the Perdew–Burke–Ernzerhof (PBE) exchange-correlation parameterization with the spin-polarized generalized-gradient approximation (GGA). A plane-wave basis set and the projector-augmented wave (PAW) method as implemented in the Vienna ab initio simulation package (VASP) were used.¹⁻³ It was conducted using 1 x 2 x 3 unit cell with Hubbard U parameter of $U_{\text{eff}} = 4.3$ eV for Fe ion. Also, it was performed using a standard Monkhorst-Pack

grid with 3 x 3 x 3 sampling meshes and cutoff energy of 500 eV to ensure the maximum force threshold of 0.01 eV/Å. The calculation results in the Figure 2 (c)-(d) of the main manuscript are also obtained within same conditions.

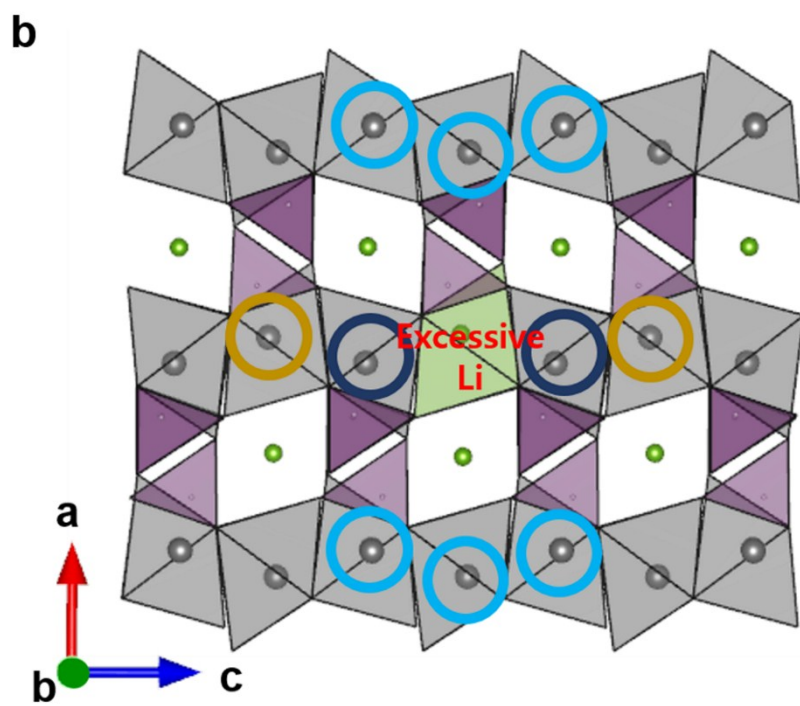
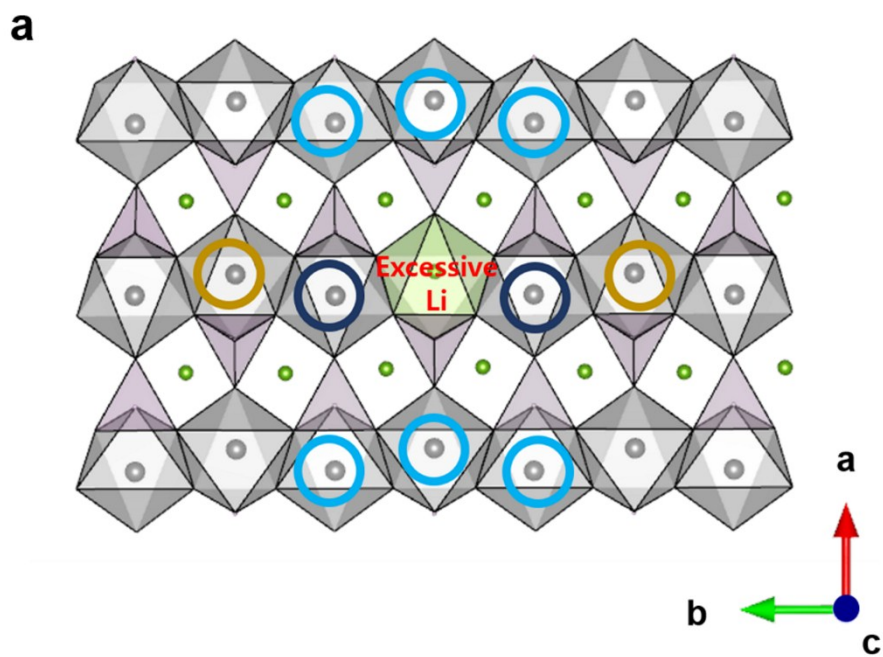


S Figure 11. The Fourier transform magnitudes of Fe K-edge EXAFS with K^3 -weight for lithium-excess LFP (red) and normal LFP (black). The Fe-P peaks of both LFPs are almost identical, but the first peak of lithium-excess LFP exhibits lower and broader intensity than that of the normal LFP. This observation could be well explained by the local structural change and the difference in Fe oxidation state of lithium-excess LFP. It is widely known that the EXAFS spectra is strongly affected by the lattice distortion as well as the oxidation state of transition metal⁴ When the coordination relationship between the absorber ions (Fe) and the coordinating ions (O or P) become non-uniform, the related peak shows broadening effects and the peak intensity decreases. In addition, it is well known that the reduction of Fe-O bond peak intensity occurs as the charge state increases⁵. The DFT calculation reveals that the excessive lithium ions in LFP should be accompanied by Fe^{3+} ions in order to maintain charge neutrality as discussed at the main manuscript. Such result indicates that the overall degree of structural disorder around Fe ions is increased at the lithium-excess LFP as well as the average Fe oxidation state, which is consistent with the EXAFS results.

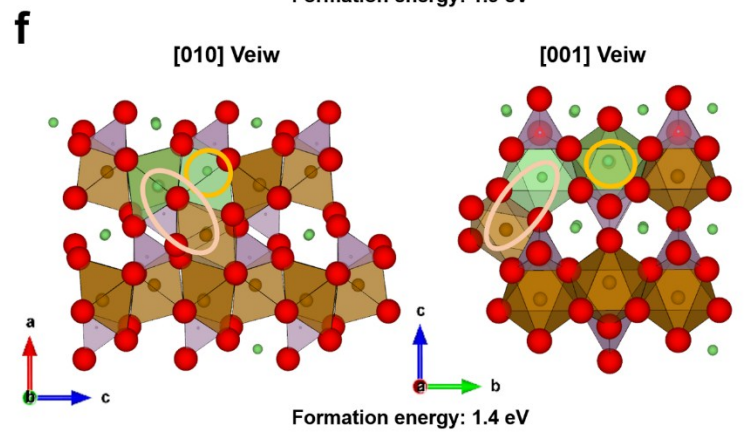
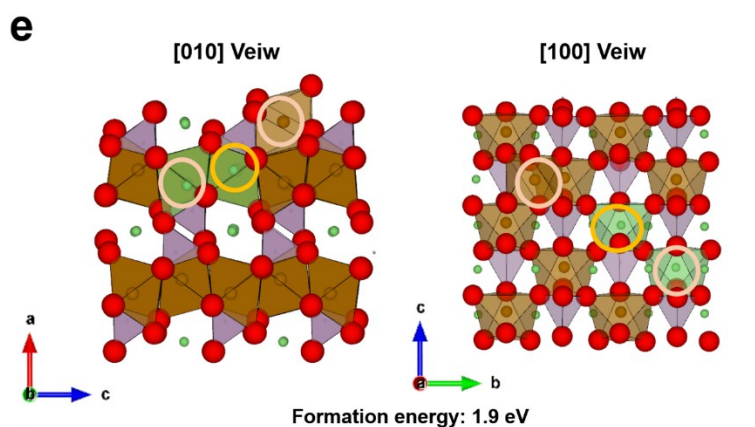
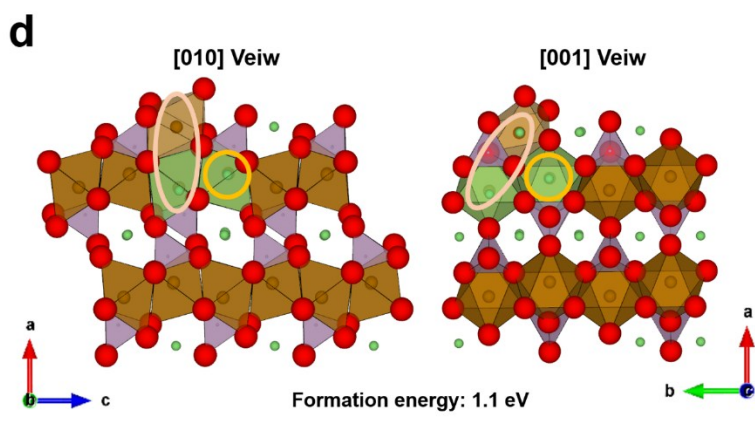
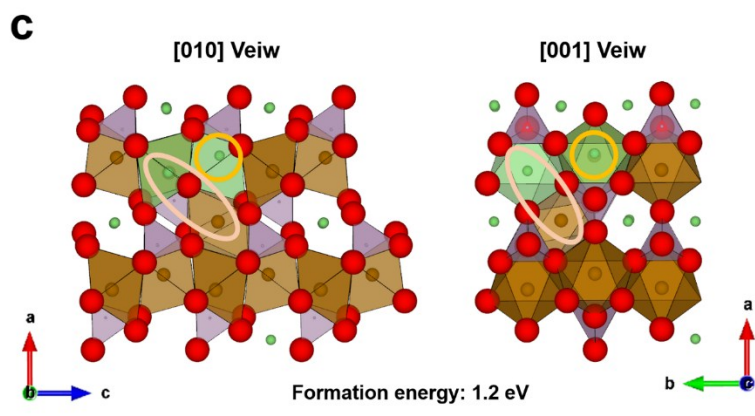


S Figure 12. *In-situ* temperature controlled XRD patterns at Ar condition of (a) 5 % lithium-excess LFP and (b) normal LFP. Over the 700 °C, the lithium-excess LFP shows Li_3PO_4 and $\text{Li}_3\text{Fe}_2(\text{PO}_4)_3$ impurities marked by asterisks. Figure (c) and (d) show the intensity ratio change before (black) and after (red) heat treatment at 700 °C of lithium-excess (c) and normal LFPs

(d) at room temperature respectively. Before treatment, the intensity ratios of both samples (black lines) are quite different, however, after treatment, these become similar. (red lines) It indicates that the lithium-excess LFP decomposed to stable normal LFP phase and impurities after 700 °C heat treatment. (e) XRD patterns of 5% lithium-excess with various synthesis conditions. The final sintering process temperature and reaction times are noted for each XRD patterns in the figure.

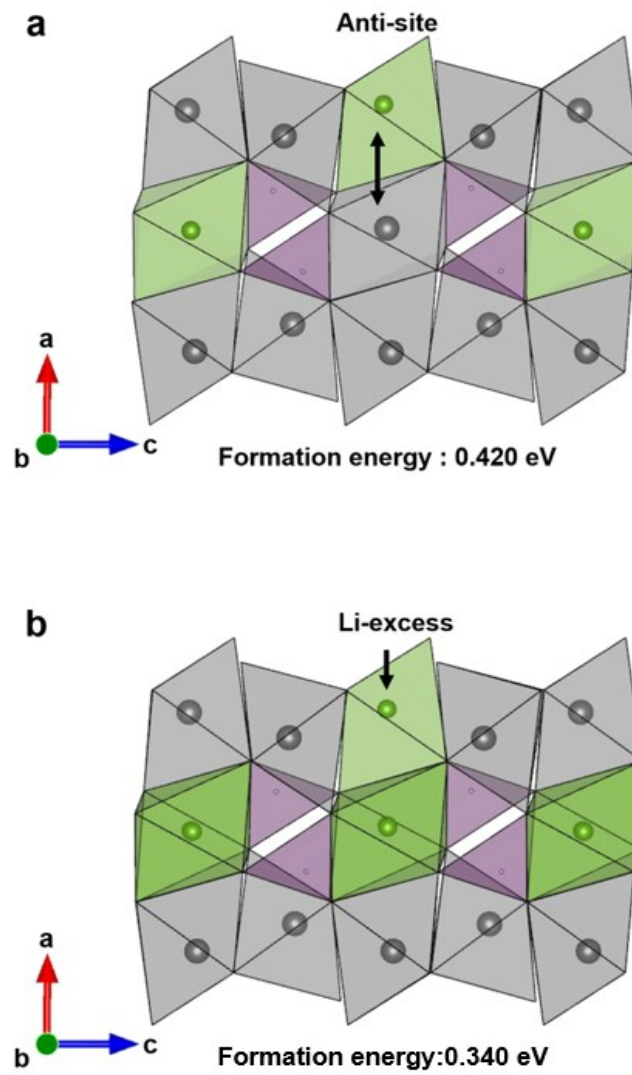


-  First neighbor Fe ions (4)
-  Second neighbor Fe ions along *a*-axis (9)
-  Second neighbor Fe ions along *b*- or *c*-axis (9)

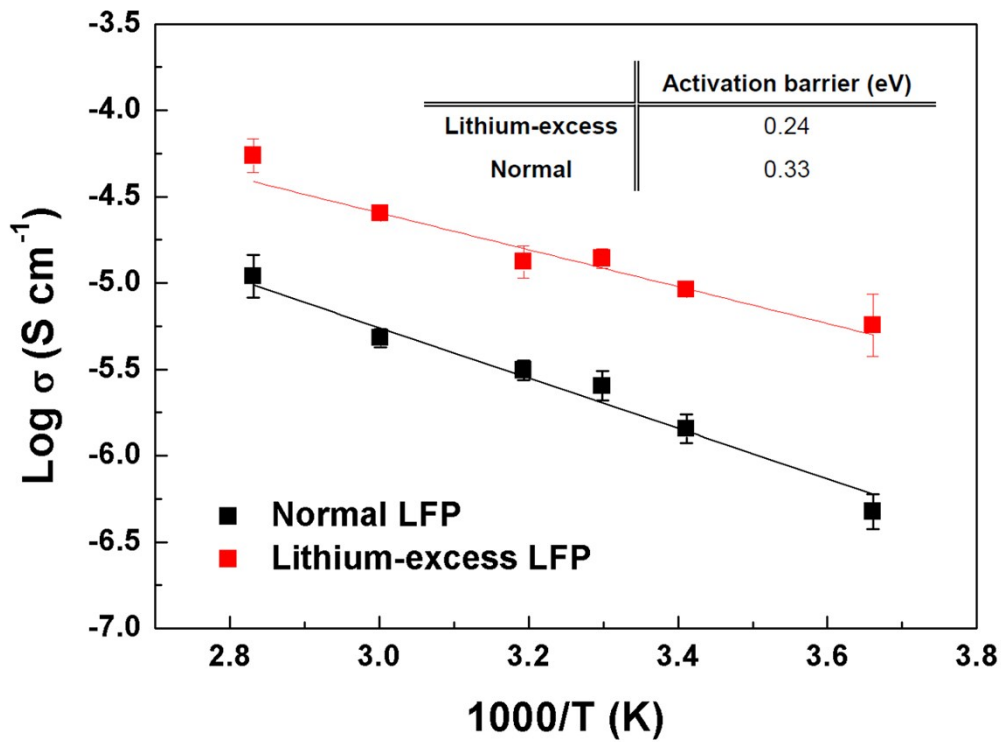


○ $\text{Li}_{\text{Fe}}\text{-Fe}_{\text{Li}}$ anti-site
 ○ Li_{Li}

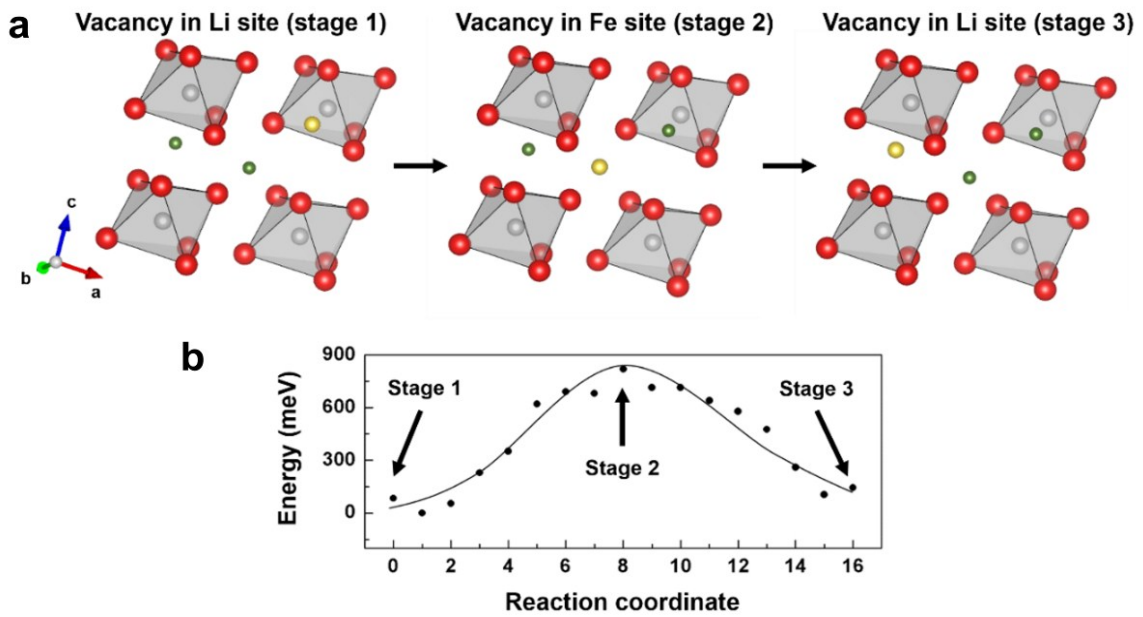
S Figure 13. Possible cation exchange sites ($\text{Li}_{\text{Fe}}\text{-Fe}_{\text{Li}}$ anti-site) at lithium-excess phase. Each figures shows a plane schematic figure of lithium-excess LFP along (a) c -axis and (b) b -axis. The sites are categorized by 3 kinds; i) First neighbor Fe ions, (marked by deep blue circle) ii) second neighbor Fe ions along a -axis (marked by sky blue circle) and iii) second neighbor Fe ions along b - or c -axis (marked by earthy yellow) of excessive Li ion. The numbers in parentheses indicate number of possible sites. (c), (d), (e) and (f) exhibit the representative $\text{Li}_{\text{Fe}}\text{-Fe}_{\text{Li}}$ pairing anti-site configuration in lithium-excess LFP which are calculated at our work. The pink and yellow circles indicate $\text{Li}_{\text{Fe}}\text{-Fe}_{\text{Li}}$ pairing anti-site and excess lithium ion respectively. DFT calculations were performed using the Perdew–Burke–Ernzerhof (PBE) exchange-correlation parameterization with the spin-polarized generalized-gradient approximation (GGA). A plane-wave basis set and the projector-augmented wave (PAW) method as implemented in the Vienna ab initio simulation package (VASP) were used.¹⁻³ It was conducted using 1 x 2 x 3 unit cell with Hubbard U parameter of $U_{\text{eff}} = 4.3$ eV for Fe ion. Also, it was performed using a standard Monkhorst-Pack grid with 2 x 2 x 2 sampling meshes and cutoff energy of 500 eV to ensure the maximum force threshold of 0.05 eV/Å. The calculation results in the Figure 2 (e)-(f) of the main manuscript are also obtained within same conditions.



S Figure 14. (a) Typical anti-site configuration and formation energy in normal LFP phase and (b) lithium-excess local configuration and formation energy.

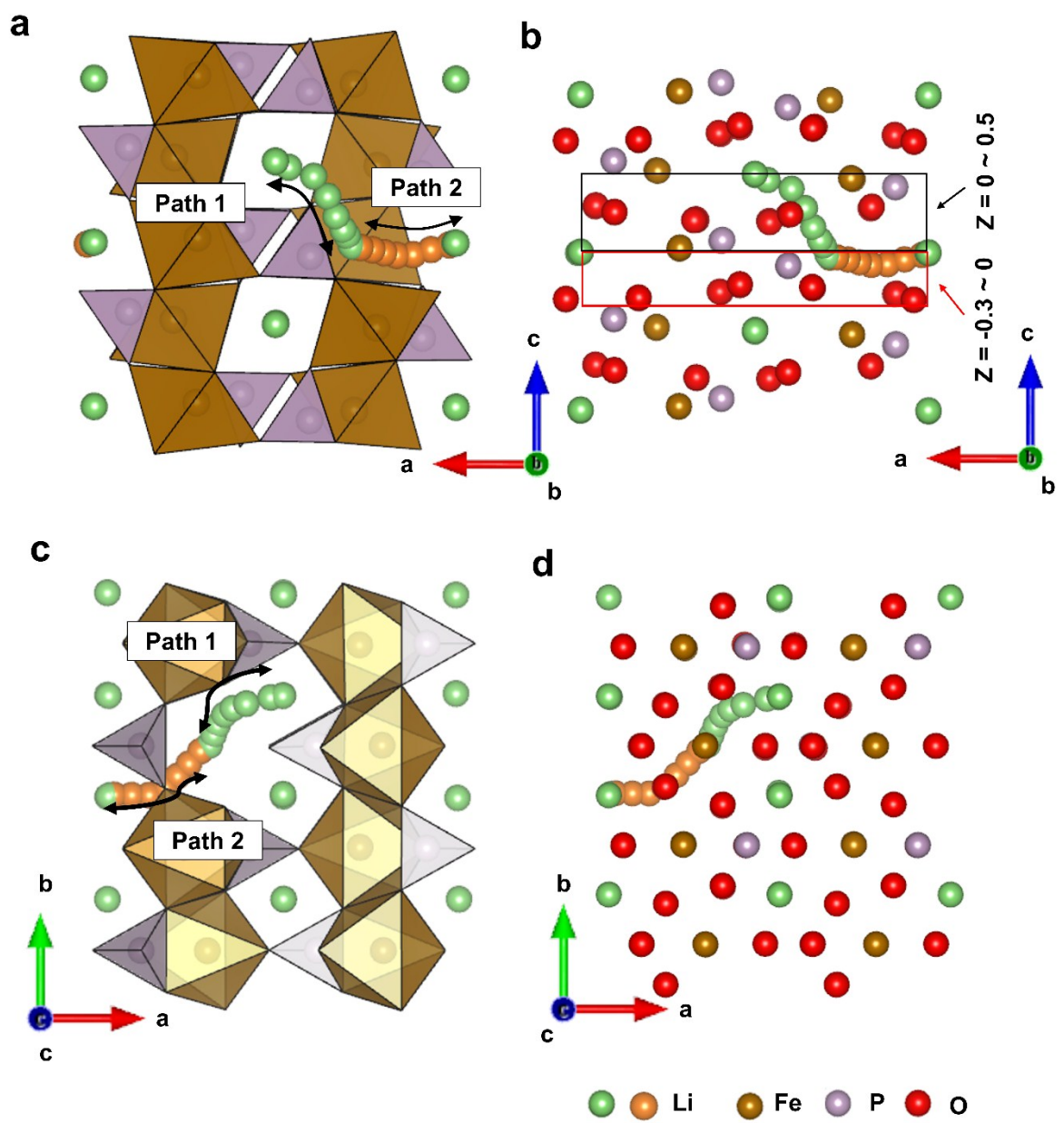


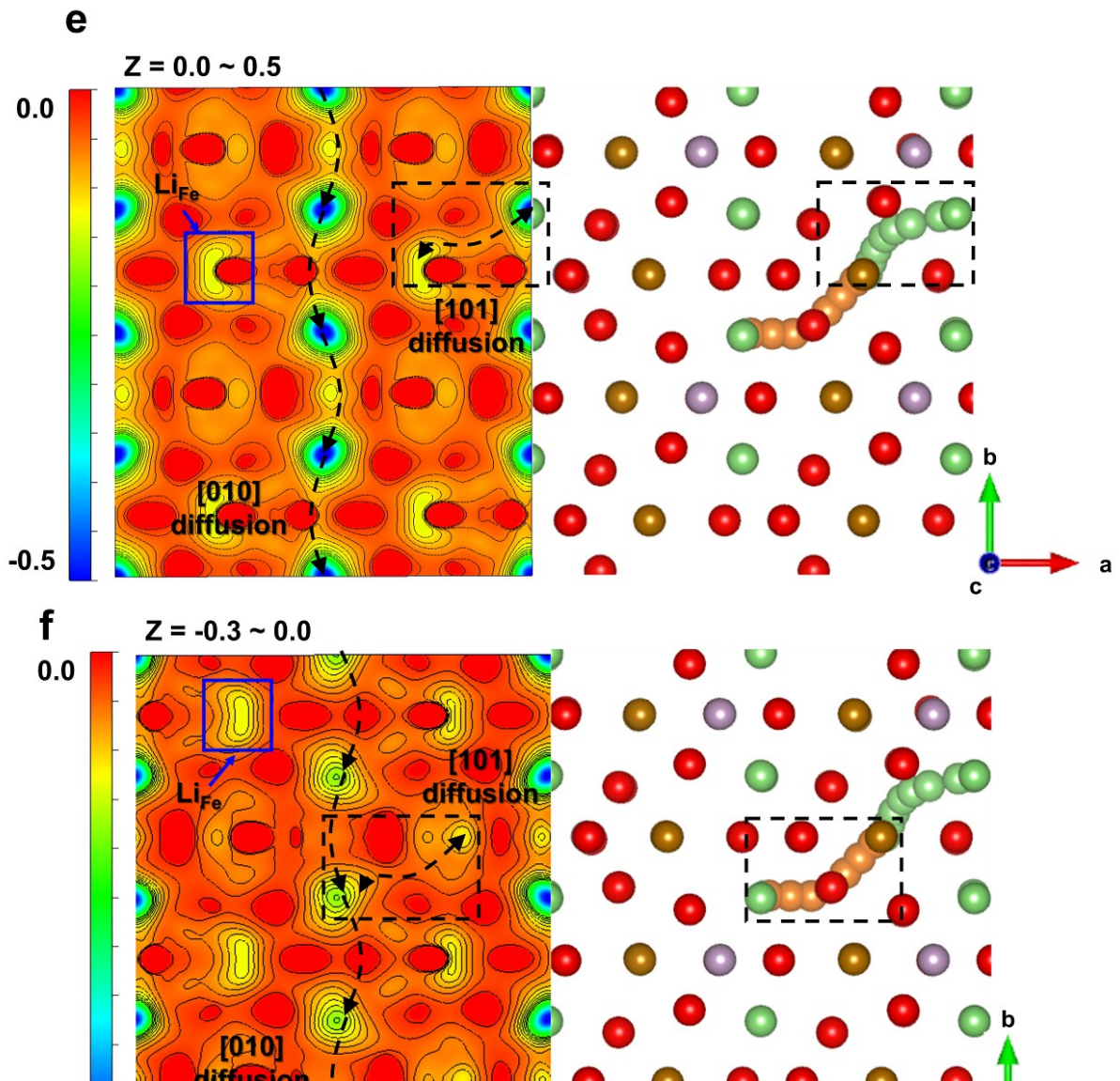
S Figure 15. Total conductivity change of Li-excess and normal LFPs at 0, 20, 30, 40, 60 and 80 °C. The EIS measurements were conducted with 3 MHz ~ 0.1 Hz using Ag/sample/Ag symmetric cells. The Li ion diffusion activation barrier is calculated based on thermal driven conductivities. The activation barriers are obtained as 240 and 330 meV for lithium-excess and normal LFP, respectively.



S Figure 16. (a) The schematics of [101] direction vacancy diffusion stages in lithium-excess LFP with activation energies. Stage 1: vacancy in Li site, stage 2: vacancy in Fe site and stage 3: vacancy in another Li site. (Green: Li atoms, purple: PO₄ tetrahedral unit, dark gray: FeO₆ octahedral unit, yellow: vacancy) (b) The activation barriers of [101] diffusion vacancy diffusion motions. We used nudged elastic band (NEB) method⁶ to determine the activation barrier of lithium ion diffusion in LFP and lithium-excess LFP. For better convergence in lithium-excess LFP, we performed GGA calculation as it shows similar activation barrier to GGA+U method in LFP⁷ and results in better energy convergence in lithium-excess LFP. In order to avoid the imaginary interaction between the unit cells in periodic boundary condition (PBC), a supercell of eight formula units (LFP: Li₃₂Fe₃₂P₃₂O₁₂₈, lithium-excess LFP: Li₃₃Fe₃₁P₃₂O₁₂₈) was introduced. Before NEB calculations, we performed a full geometric relaxation of LFP and lithium-excess LFP with free lattice parameters and internal degrees of freedom. Then, a single lithium vacancy was generated to describe the lithium vacancy diffusion in each supercell. After setting initial and final images, NEB calculations with seven

intermediate images were conducted with fixed lattice parameters and free internal degrees of freedom. To avoid the drift of images by the fake force, we fixed lattice parameters during NEB calculations as suggested by VASP code. Since the lattice parameters were optimized before the NEB calculations, we believe that the errors caused by fixed lattice constants during NEB calculations are negligible, resulting in limited amount of errors on the NEB barriers. The calculations with an energy cutoff of 500 eV and a single k -point were performed until the free energy converges within 0.05 eV per unit cell. The calculation results in the Figure 3 of the main manuscript is also obtained within same conditions.





S. Figure 17. The proposed [101] diffusion path of lithium-excess LFP schematically shown in the ac plane (a, b) and the ab plane (c, d). Figure (a) and (c) exhibit the polyhedron framework corresponding with (b) and (d) figures, respectively. (Li: green and orange, Fe: brown, P: purple and O: red atoms) The path 1 (Li_{Li} to Li_{Fe}) and path 2 (Li_{Fe} to Li_{Li}) diffusion paths are depicted with green and orange atoms, respectively. The black and red rectangle box in the figure (b) presents the Maximum entropy method (MEM) analysis range for figure (e) and figure (f), respectively. The MEM analysis (right) and proposed diffusion path by DFT

calculation (left) of path 1 (e) and path 2 (f). (The path 1 and path 2 are represented by green and orange atoms, respectively) The figure (e) and (f) are projected MEM analysis results from $z = 0.0$ to $z = 0.5$ and from $z = -0.3$ to $z = 0.0$, respectively. (See figure (b)) The iso-surface level of MEM analysis is only considered negative atomic scattering values from 0 to -0.5.

Detail experimental condition and discussion on MEM analysis

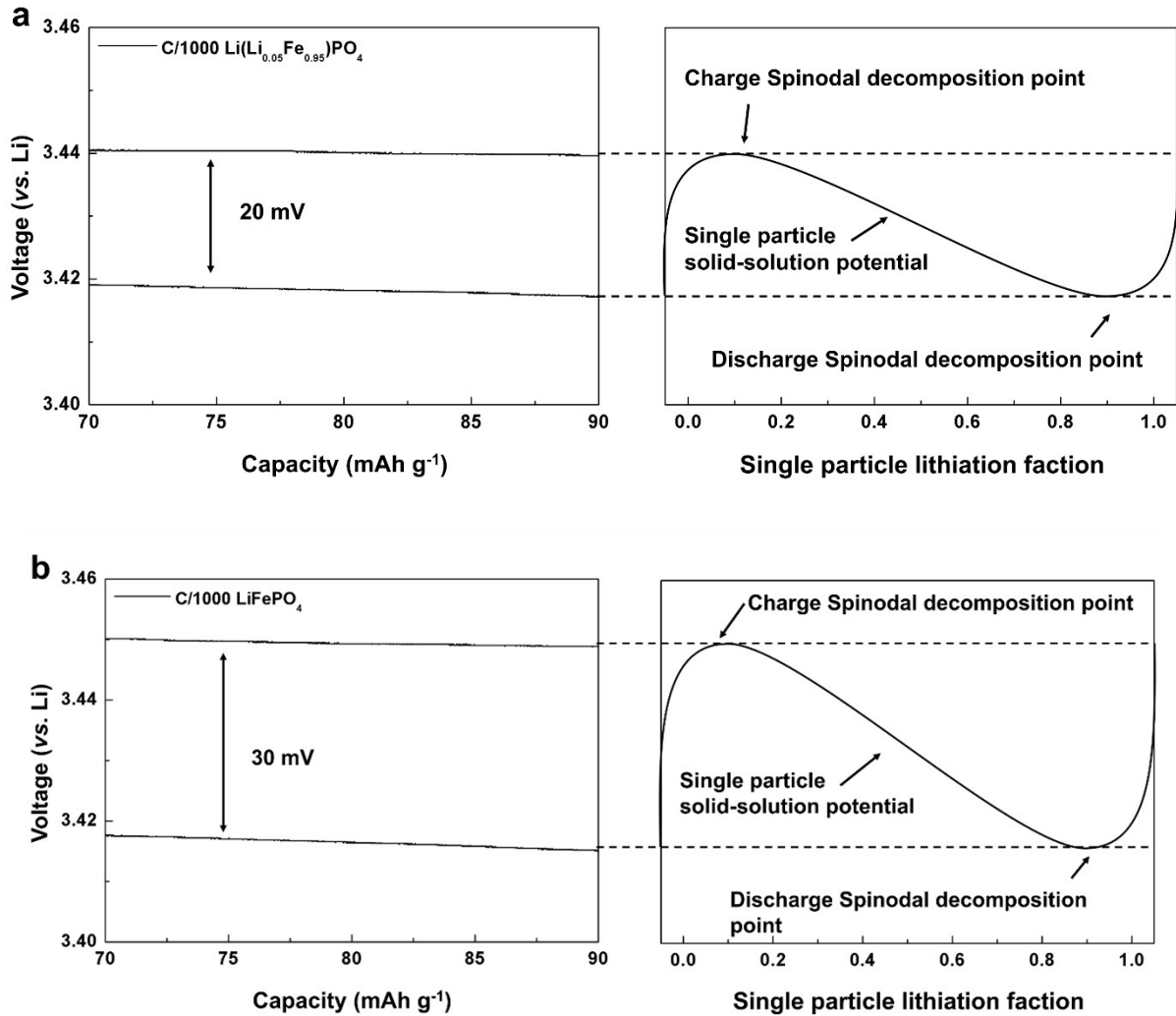
Method

The fully delithiated lithium-excess FP was firstly prepared using nitronium tetrafluoroborate (NO_2BF_4) as an oxidizing agent. A 1.5 fold excess of NO_2BF_4 was dissolved in acetonitrile before adding lithium-excess LFP powders, and stirred for 24 h at Ar atmosphere. The mixture was filtered and washed several times with acetonitrile before drying under vacuum. The partially delithiated lithium-excess LFP is prepared by mixing of lithium-excess LFP and delithiated lithium-excess FP with 2:1 molar ratio. The neutron diffraction patterns were obtained using fixed wave length at 370 °C under vacuum condition. The iso-surface level of MEM analysis considers only negative atomic scattering values from 0 to -0.5. The positive value iso-surface level (which means depiction of Fe, P and O ions) is not considered to avoid summation between positive and negative iso-surface signals. The transition metal, P, O and background level (zero iso-surface level) are depicted as a red color.⁸

Discussion

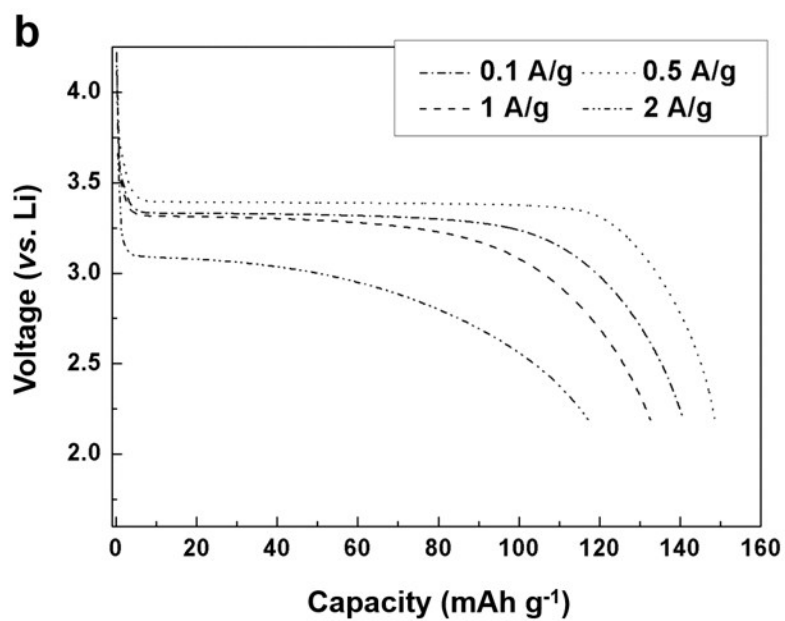
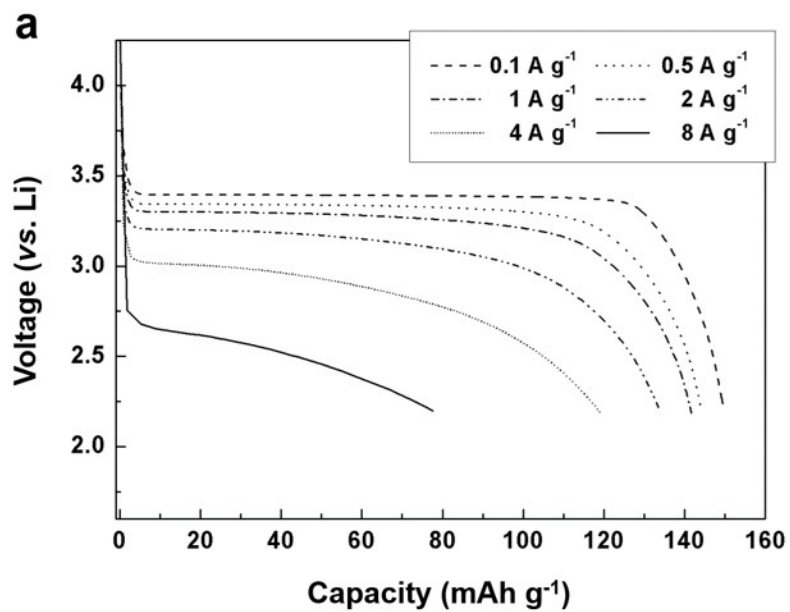
The S figure 17 (a)-(b) set and (c)-(d) set illustrate the [101] diffusion path suggested by DFT calculations shown schematically in the *ac* plane and the *ab* plane, respectively. S figure 17 (a) and (c) display the polyhedron framework corresponding with (b) and (d) figures, respectively. (Li: green and orange, Fe: brown, P: purple and O: red atoms) The [101] diffusion path can be divided into the path 1 (Li_{Li} to Li_{Fe} , green atoms) and path 2 (Li_{Fe} to Li_{Li} , orange atoms) as shown in S figure 17 (a), and we investigated each path 1 and path 2, separately, to prevent the overlapping depiction of each diffusion paths during MEM analysis. S figure 17 (e) is a projected atomic density from $z = 0$ to $z = 0.5$ (z is equal to the *c*-axis parameter of *Pnma* unit cell), corresponding to the black rectangular box in S figure 17 (b). The S figure 17 (e) shows

that MEM analysis clearly detects the atomic density of lithium ions in the Fe site (Li_{Fe} denoted with a blue box), and, more importantly, the atomic density of lithium ions are also obviously detected within the [101] diffusion path corresponding to the path 1. This figure evidently exhibits the Li in Fe site (Li_{Fe}), supporting the lithium-excess in the LFP crystal structure. Moreover, it indicates that the lithium ions in the Fe site and the original Li site are well connected with the thermal vibration, and this continuous lithium signals from Li_{Li} site to Li_{Fe} site supports a diffusion path along the direction matching with the suggested diffusion path 1 by DFT calculation as depicted beside MEM image. In addition to [101] path, [010] diffusion path which has been regarded as the main path in the LFP is also observed with more atomic density along it. The brighter image along [010] compared to [101] path is due to the faster Li motion along [010]. Similar observation to the path 2 in the lithium-excess LFP was also made as shown in S figure 17 (f), which corresponds to the projection image from $z = -0.3$ to $z = 0$. The iso-surface of lithium atomic density along the [101] direction is comparatively observable to that of the [010] direction, even though the intensity is not as high as the region of $z = 0 \sim 0.5$.

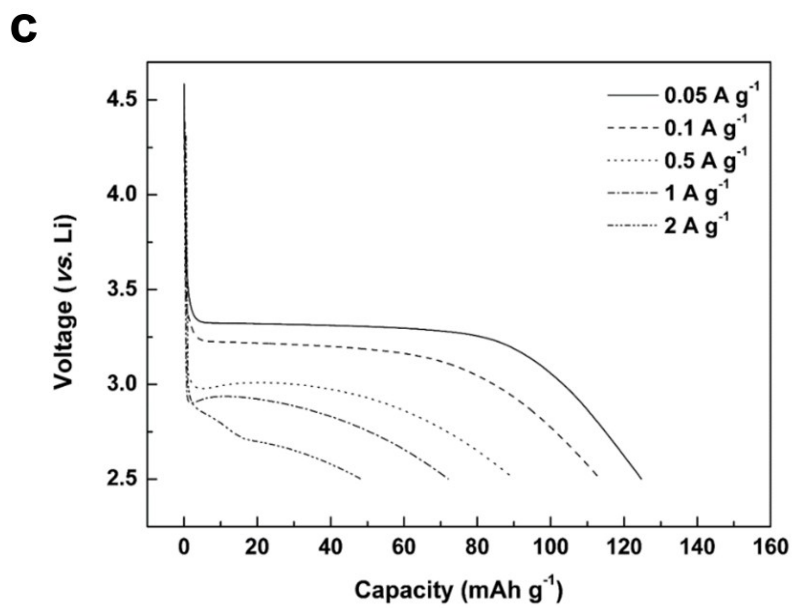
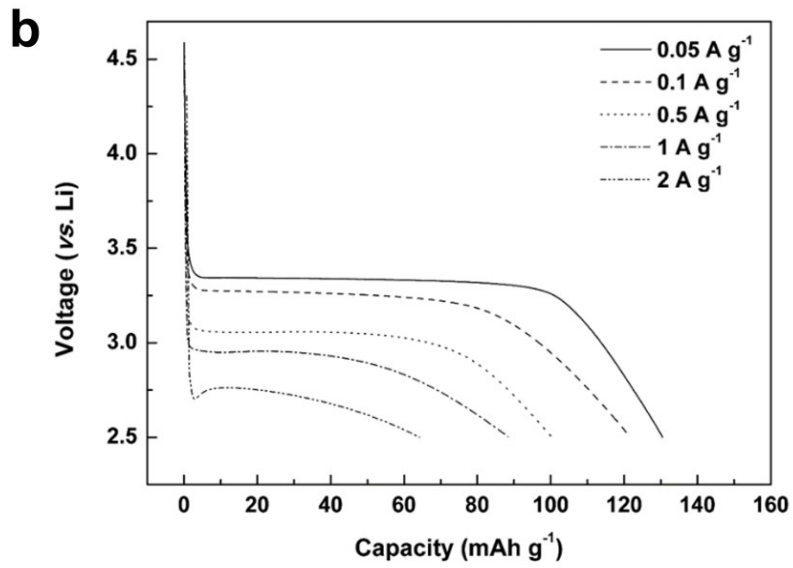
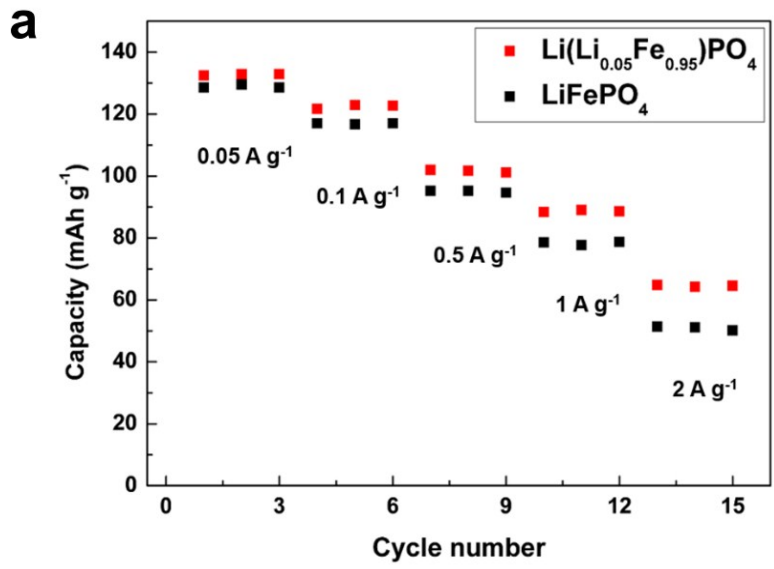


S Figure 18. (a) and (b) show the relationship between CC profiles with a C/1000 current density and single particle solid-solution behavior of lithium-excess and normal LFP electrodes, respectively. The voltage gaps between charge and discharge with a near-zero current density is explained by many-body particle models with single particle solid-solution behavior.⁹ The highest of del/lithiation Spinodal decomposition points (phase transition activation barrier) are strongly related with positive energy penalties induced from coherency/interfacial energies at a moderate particle size. Recently, there is growing evidence that the phase transition barrier could be decreased by nano-sizing,¹⁰ doping¹¹ and transition

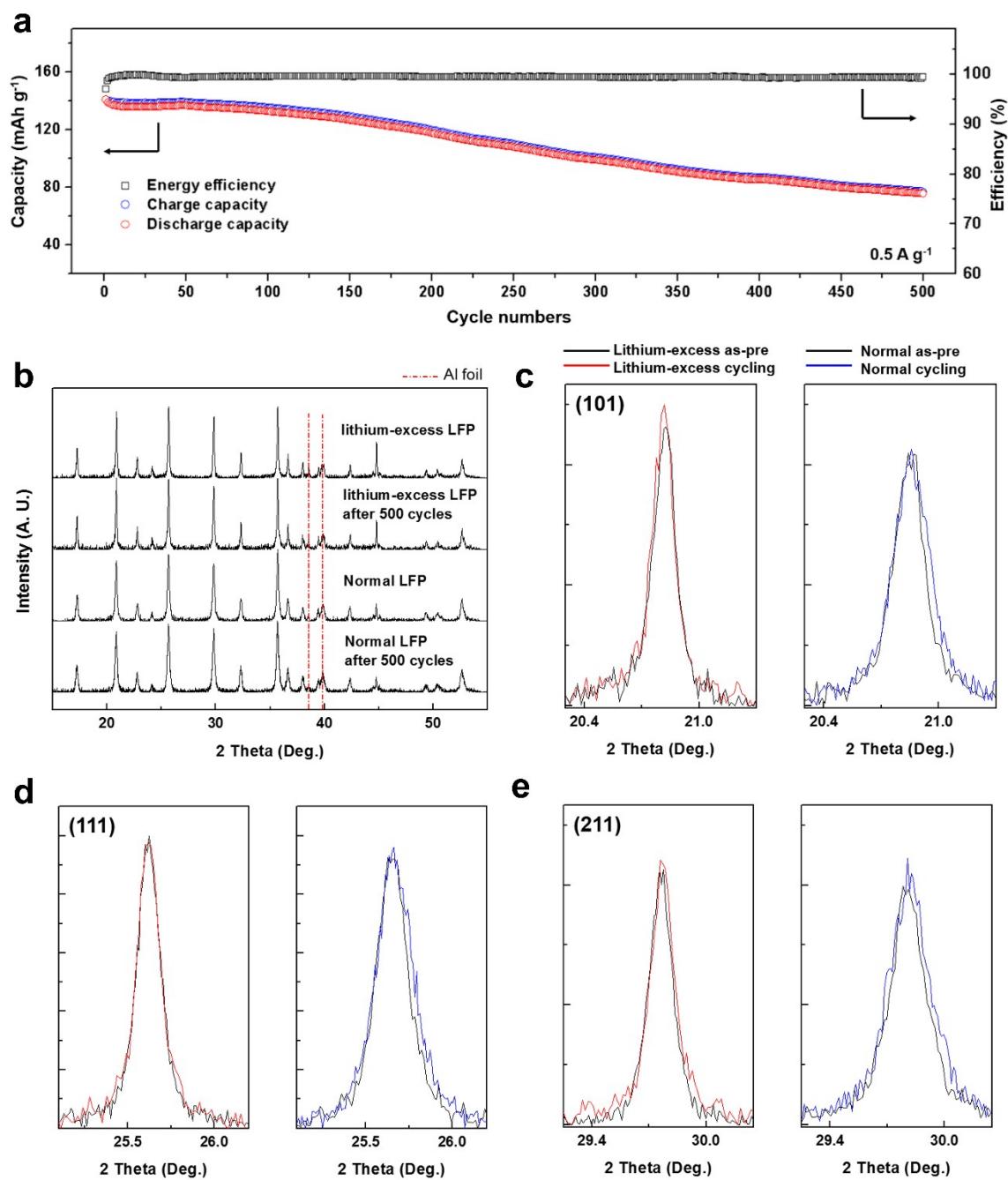
metal substitution.¹²



S Figure 19. Galvanostatic discharge profiles of lithium-excess LFP (a) and normal LFP (b) at various current rates.

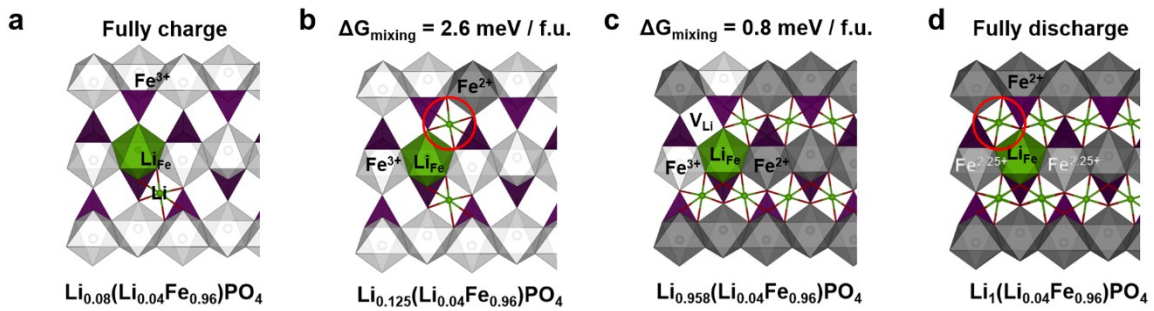


S Figure 20. (a) Rate capability of lithium-excess LFP (red) and normal LFP (black) at 0 °C. Figure (b) and (c) show the discharge profiles of the lithium-excess and the normal LFPs, respectively. The lithium-excess LFP still exhibits higher rate performance than normal LFP at 0 °C. Lithium-excess LFP delivers a discharge capacity of ~ 66 mAh g⁻¹ at a current density of 2 A g⁻¹, which is ~ 30 % higher than that of normal LFP (~ 49 mAh g⁻¹) at the same current density. Also, the polarization of lithium-excess LFP is much lower than that of normal LFP. For example, the average discharge voltages of lithium-excess and normal LFPs are observed as 3.06 V and 3.01 V, respectively, at the current density of 0.5 A g⁻¹.



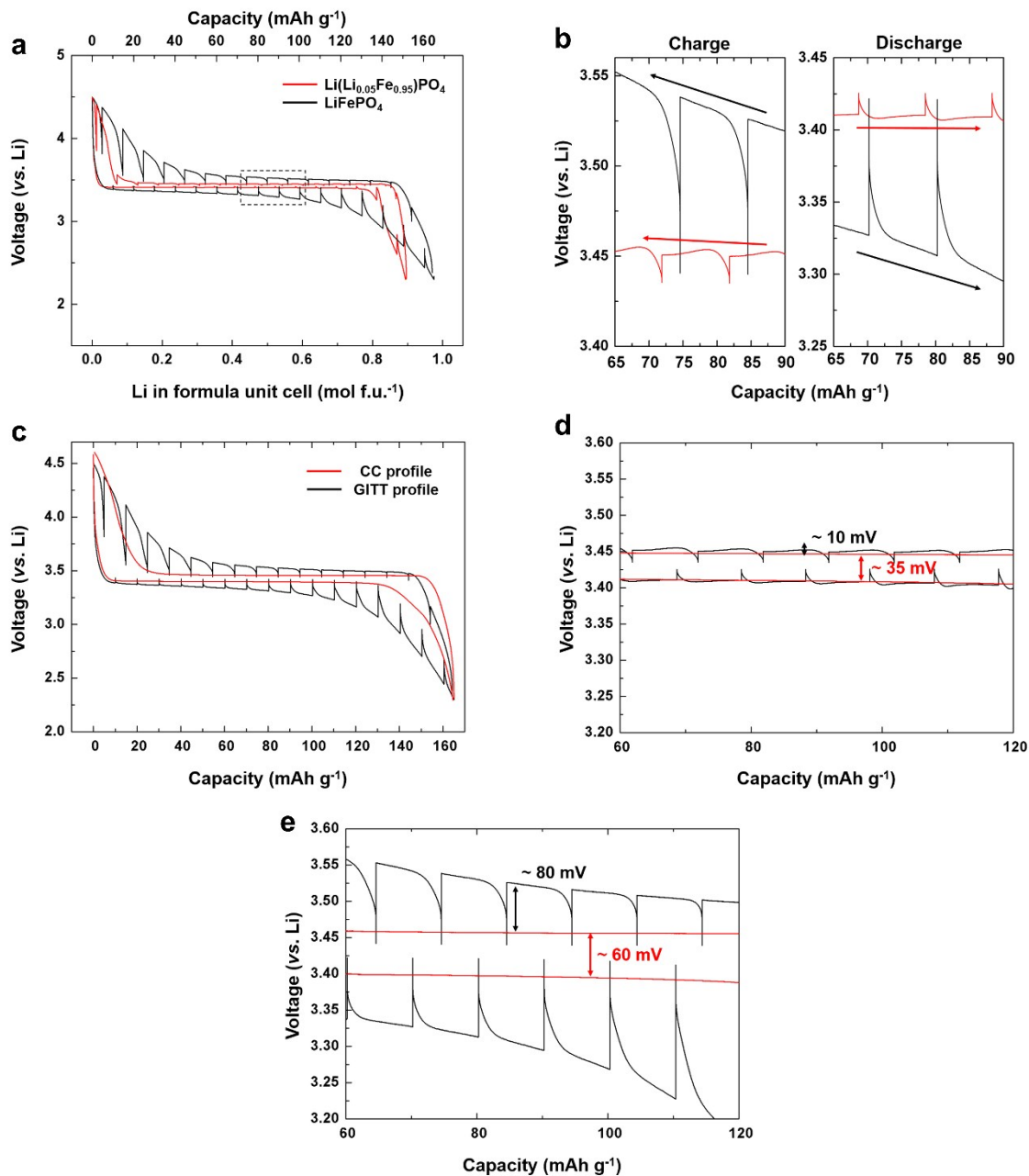
S Figure 21. (a) Cycle life test of normal LFP with a current density 0.5 A g^{-1} . (Corresponding with 2.95 C) The capacity after 500 cycles maintained 58.4 % of the initial charge/discharge capacity. The S Figure 21 (b) shows the XRD patterns of as-prepared lithium-excess LFP, lithium-excess LFP after 500 cycles, as-prepared normal LFP and normal LFP after 500 cycles,

respectively. Both LFP electrodes exhibit insignificant XRD pattern changes after cycling as shown in S Figure 21 (b). However, as shown in zoomed-in figures (c), (d) and (e) for (101), (111) and (211) peaks, respectively, the peak broadening of normal LFP electrode (blue) is observable after cycling compared with as-prepared LFP (black) electrode, while the lithium-excess LFP (red) electrode maintains its peak shape after cycling. It is well known that the broadening of diffraction peak is mainly attributed from non-uniform distribution of local strain or particle size reduction¹³, clearly indicating that the structural degradation of normal LFP occurs after cycling, whereas the initial structure of lithium-excess LFP is relatively well maintained. According to recent research¹⁴, the local current density, which is induced from the phase transformation barrier height, strongly affects the cycle-life because it leads to the non-uniformity phase transition reaction on the electrode. In the case of LFP, Spinodal decomposition barrier mainly determines the degree of local current density, therefore, a lower Spinodal decomposition barrier could make the phase transition more uniform, leading to the cycle-life enhancement. In this respect, we believe that the higher capacity retention of lithium-excess LFP than that of normal LFP is mainly attributed to the lowered Spinodal decomposition barrier as discussed in the manuscript.

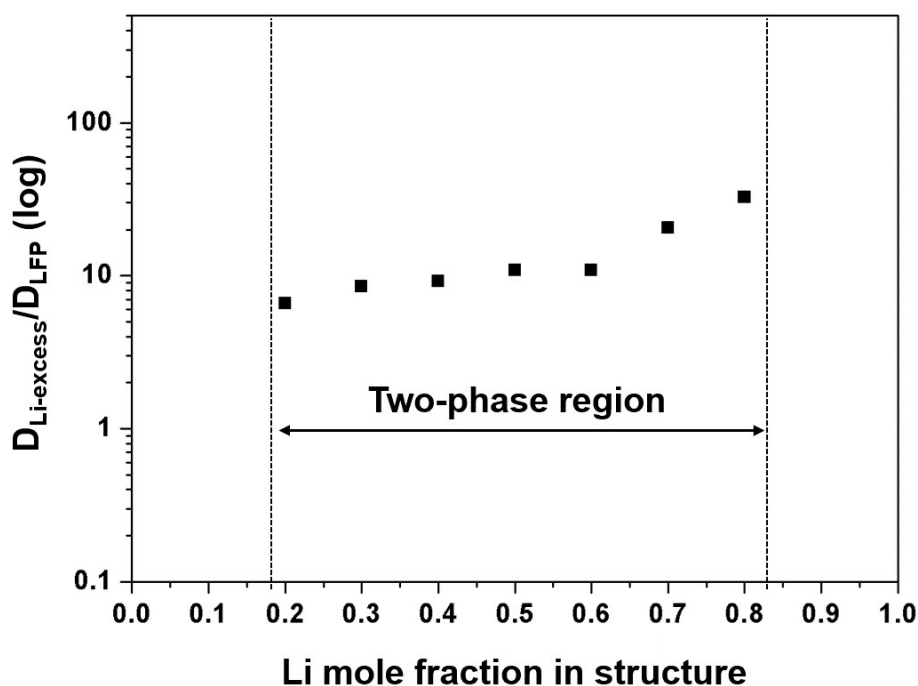


S Figure 22. It is revealed by DFT calculation that the unique Li-excess atomic configuration has preferred interstitial sites to extract or insert Li ions during Li concentration change. The Figure (a) – (d) show local Li-excess configuration corresponding with the lowest mixing energy at certain Li fractions. At the end of charge state, (Figure (a)) Li_{Fe} ion and another Li_{Li} ion remained due to all Fe ions oxidized to 3+ state. And, when an electron is inserted into electrode, the additional Li ion is located at near Li-excess configuration site marked with red circle in Figure (b) with 2.6 m eV f.u.⁻¹ mixing energy. Similarly, at the beginning of discharge state, the Li ion marked by red circle in Figure 5 (d) is firstly came out with 0.8 meV f.u.⁻¹ phase mixing energy. (Figure 5 (c)) Although we could not investigate mixing energy for whole Li concentration and precise Li composition of solubility limits due to limitation of DFT calculation, this result elucidates that the lithium-excess LFP has energetic lower alternative diffusional configuration than normal LFP because Li-excess local configuration plays role as a “*phase mixing seed*”. DFT calculations were performed using the Perdew–Burke–Ernzerhof (PBE) exchange-correlation parameterization with the spin-polarized generalized-gradient approximation (GGA). A plane-wave basis set and the projector-augmented wave (PAW) method as implemented in the Vienna ab initio simulation package (VASP) were used.¹⁻³ We used a Hubbard U parameter of $U_{\text{eff}} = 4.3$ eV for Fe ion. Calculations were performed using a standard Monkhorst-Pack grid with cutoff energy of 500 eV and 2 x 2 x 1 sampling meshes to

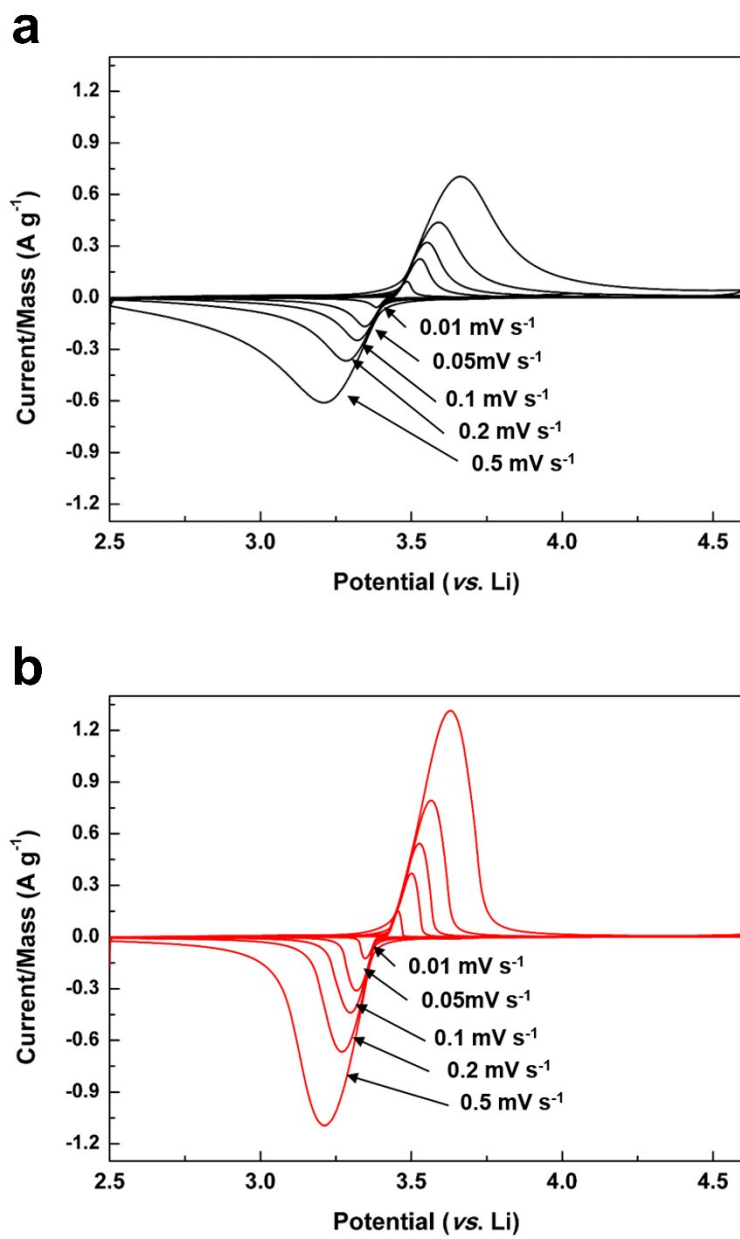
ensure the maximum force threshold of 0.05 eV/Å. Configuration conditions: 1 or 2 vacancy for $\text{Li}_{24-x}[\text{Fe}_{23/24}\text{Li}_{1/24}](\text{PO}_4)_{24}$ cell ($x = 1$ or 2) and 1 or 2 lithium ion for $\text{Li}_x[\text{Fe}_{23/24}\text{Li}_{1/24}](\text{PO}_4)_{24}$ cell ($x = 1$ or 2)



S Figure 23. (a) Comparison of GITT profiles of lithium-excess and normal LFPs. (b) Magnified GITT charge and discharge profiles. It is observed that the normal LFP shows high polarization at GITT compared with CC mode as shown in (c). Polarization differences between GITT and CC mode is obtain as under 10 mV and over 80 mV at lithium-excess and normal LFPs, respectively, as shown in (d) and (e).



S Figure 24. The effective diffusivity ratio ($D_{\text{Li-excess}}/D_{\text{LFP}}$) calculated from GITT results with in two-phase reaction region.¹⁵ The lithium-excess LFP shows statically 10 times higher diffusivity than normal LFP. The diffusivity estimated from the GITT measurement is only for the qualitative comparison and does not represent the fundamental properties of electrodes operating *via* two-phase reaction, since the single diffusivity cannot be defined in such two-phase reaction. Thus, the information from the figure should be taken with care.



S Figure 25. Cyclic voltammetry of (a) normal LFP and (b) lithium-excess LFP with various scan rate.

	Normal LFP	Lithium-excess LFP
Anodic D ($\text{cm}^2 \text{s}^{-1}$)	$3.22 (3) \times 10^{-15}$	$2.01 (2) \times 10^{-14}$
Cathodic D ($\text{cm}^2 \text{s}^{-1}$)	$2.50 (1) \times 10^{-15}$	$1.29 (2) \times 10^{-14}$

S table 1. The calculated diffusion constant from cyclic voltammetry measurement. The lithium-excess LFP exhibit one-order higher diffusion constant than normal LFP.

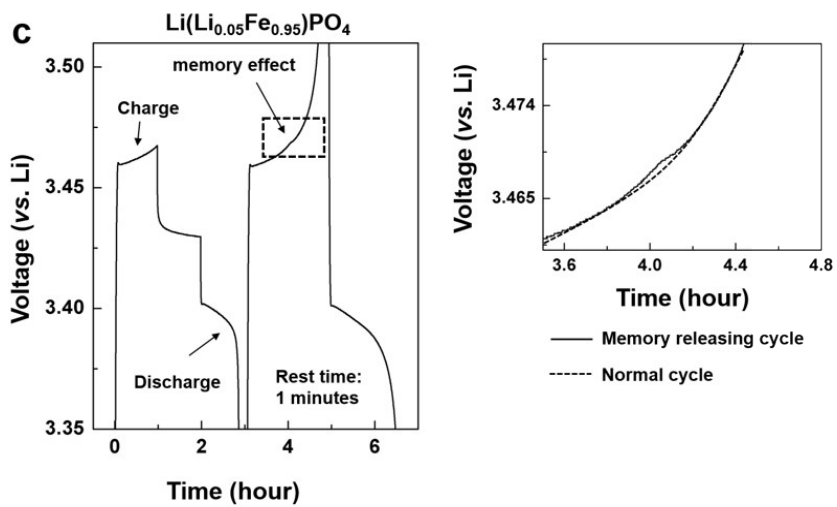
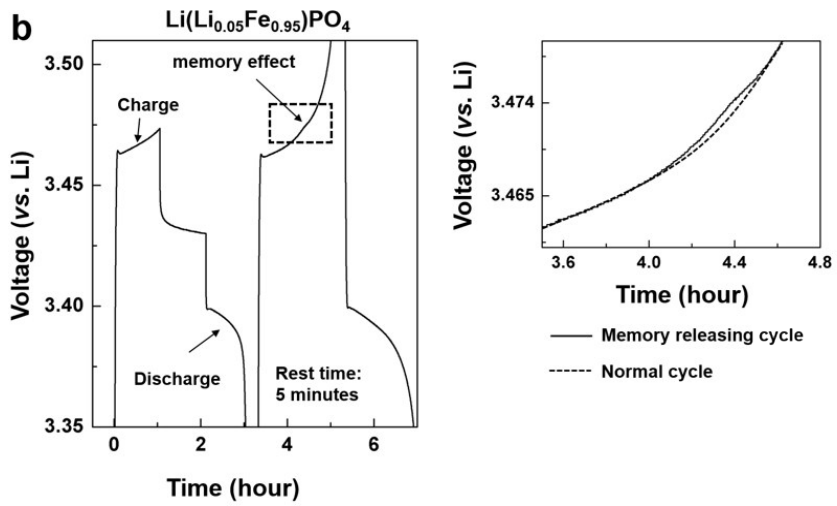
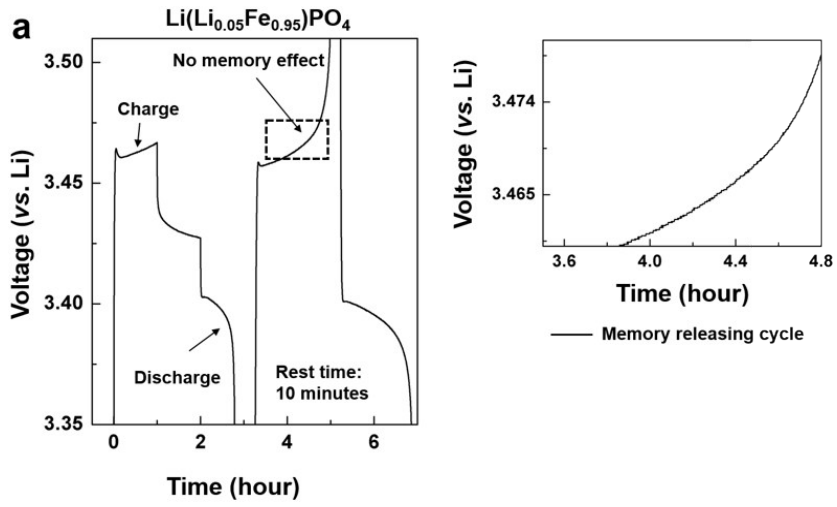
The attached S figure 25 (a) and (b) exhibit the CV analyses for the normal LFP and the lithium-excess LFP, respectively. The intensities of redox current peaks for the lithium-excess LFP are much higher than those of normal LFP for all scan rates, indicating the higher electrochemical reactivity of lithium-excess LFP. For the quantitative comparison on diffusivities of both electrodes, we calculated the apparent diffusion constants using the following equation:

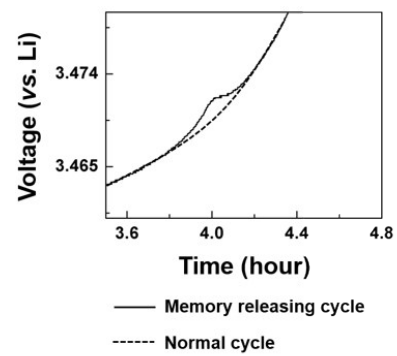
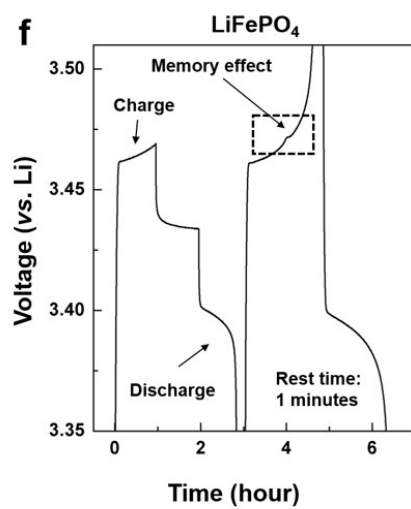
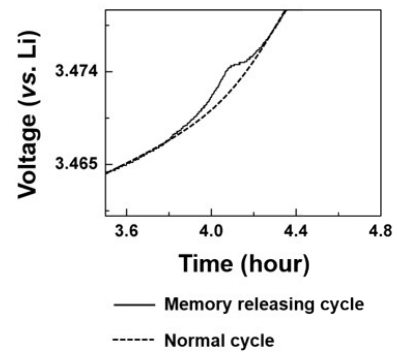
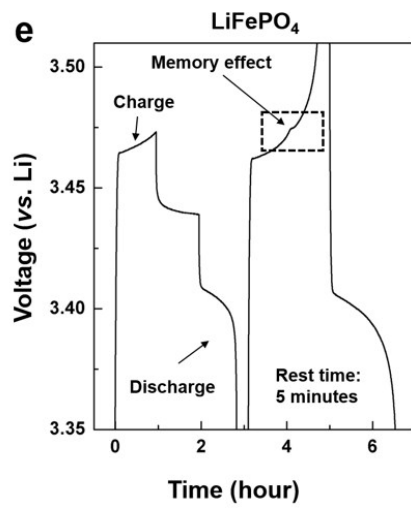
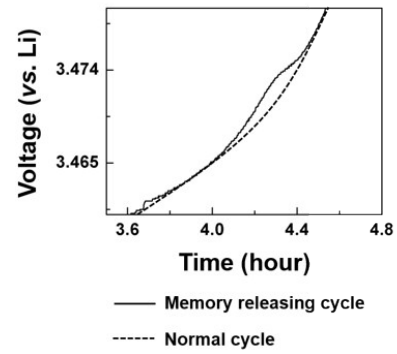
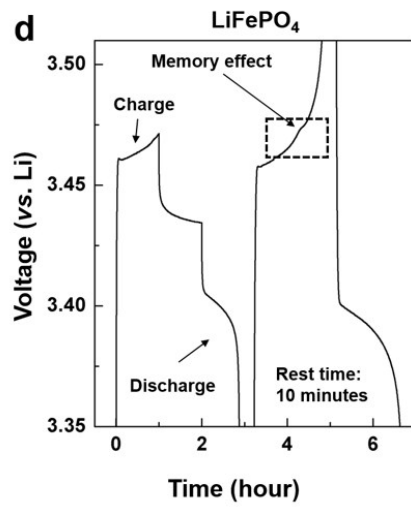
$$\frac{i_p}{m} = 0.4463F \left(\frac{F}{RT} \right)^{1/2} \nu^{1/2} C_{Li}^* A_e D^{1/2}$$

Where i_p is the peak current in amperes, F is Faraday constant, R is gas constant, T is temperature in kelvin, m is mass of the electrode, ν is the scan rate (V s^{-1}), C_{Li}^* is the initial concentration of Li in the electrode materials ($0.0228 \text{ mol cm}^{-3}$), A_e is the electrode area per unit mass (cm g^{-1}), and D is the apparent diffusion constant (cm s^{-1}). The effective electrode area of the [010] plane is taken as one-third of the total BET surface area¹⁶

The S Table 1 shows the calculated diffusion constants of both LFPs based on the CV analyses at the room temperature. The diffusion constant of normal LFP exhibits a comparable value with previous reports ($\sim 10^{-15} \sim 10^{-16} \text{ cm}^2 \text{ s}^{-1}$)^{16, 17} however, the diffusion constant of lithium-excess LFP is about one order higher than that of normal LFP. This result is consistent with the

diffusivity estimation by GITT measurement. Considering that all the components of coin-cell are identical, the higher electrochemical activity is attributed to the higher lithium ion diffusivity of the electrode material. We believe that the improved electrochemical activity of lithium-excess LFP than that of normal LFP is attributed to (i) near zero anti-site concentration, (ii) additional diffusion path of [101] and (iii) lowered Spinodal decomposition barrier as we claimed at the main-manuscript.





S Figure 26. Confirmation on memory effect depending on rest time between memory writing (first half charge/discharge) cycle and memory releasing (second full charge/discharge) cycle. The all experiments are conducted with a 80 mA g^{-1} current density and $2.5 \sim 4.5 \text{ V}$ (vs. Li) voltage windows. (a) 10 minutes rest time, (b) 5 minutes rest time and (c) 1 minute rest time for lithium-excess LFP. (d) 10 minutes rest time, (e) 5 minutes rest time and (f) 1 minute rest time for normal LFP. The memory effect is reinforced with decreasing rest time between first cycle and second cycle at both LFPs. However, the degree of overshooting of lithium-excess LFP is remarkably lower than counterpart normal LFP electrode, and the overshooting (memory effect) has completely disappeared with more than 10 minutes rest time. We infer that the fast kinetic of lithium-excess configuration makes active particles fast reunion in the relaxation state (rest state), resulting in erasing memory effect as shown in (a). Also, the relatively low phase transition activation energy of lithium-excess LFP could affect on lowering degree of overshooting compared with normal LFP as show in (b) and (c).

Reference

1. J. P. Perdew, K. Burke and M. Ernzerhof, *Phys. Rev. Lett.*, 1996, **77**, 3865-3868.
2. G. Kresse and J. Furthmüller, *Comp. Mater. Sci.*, 1996, **6**, 15-50.
3. V. I. Anisimov, J. Zaanen and O. K. Andersen, *Phys. Rev. B*, 1991, **44**, 943-954.
4. Y.-C. Chen, J.-M. Chen, C.-H. Hsu, J.-F. Lee, J.-W. Yeh and H. C. Shih, *Solid State Ion.*, 2009, **180**, 1215-1219.
5. D. Jang, K. Palanisamy, J. Yoon, Y. Kim and W.-S. Yoon, *J. Power Sources*, 2013, **244**, 581-585.
6. G. Henkelman, B. P. Uberuaga and H. Jónsson, *J. Chem. Phys.*, 2000, **113**, 9901-9904.
7. D. Morgan, A. Van der Ven and G. Ceder, *Electrochem. Solid State Lett.*, 2004, **7**, A30-A32.
8. F. Izumi and K. Momma, *IOP Conference Series: Materials Science and Engineering*, 2011, **18**, 022001.
9. W. Dreyer, J. Jamnik, C. Guhlke, R. Huth, J. Moskon and M. Gaberscek, *Nat. Mater.*, 2010, **9**, 448-453.
10. D. A. Cogswell and M. Z. Bazant, *Nano Lett.*, 2013, **13**, 3036-3041.
11. F. Omenya, N. A. Chernova, R. Zhang, J. Fang, Y. Huang, F. Cohen, N. Dobrzynski, S. Senanayake, W. Xu and M. S. Whittingham, *Chem. Mater.*, 2012, **25**, 85-89.
12. D. B. Ravnsbæk, K. Xiang, W. Xing, O. J. Borkiewicz, K. M. Wiaderek, P. Gionet, K. W. Chapman, P. J. Chupas and Y. M. Chiang, *Nano Lett.*, 2014, **14**, 1484-1491.
13. Y. Shin and A. Manthiram, *Electrochem. Solid State Lett.*, 2002, **5**, A55-A58.
14. Y. Li, F. El Gabaly, T. R. Ferguson, R. B. Smith, N. C. Bartelt, J. D. Sugar, K. R. Fenton, D. A. Cogswell, A. L. D. Kilcoyne, T. Tyliczszak, M. Z. Bazant and W. C. Chueh, *Nat. Mater.*, 2014, **13**, 1149-1156.
15. P. P. Prosini, M. Lisi, D. Zane and M. Pasquali, *Solid State Ion.*, 2002, **148**, 45-51.
16. K. Tang, X. Yu, J. Sun, H. Li and X. Huang, *Electrochim. Acta*, 2011, **56**, 4869-4875.
17. L. Li, X. Tang, H. Liu, Y. Qu and Z. Lu, *Electrochim. Acta*, 2010, **56**, 995-999.